A critical review of magnesium silicate hydrate (M-S-H) phases for binder applications

Harisankar Sreenivasan [a], Ellina Bernard [b], Hellen S. Santos [a], Hoang Nguyen [a,b], Samira Moukannaa [a], Adeolu Adediran [a], John L. Provis [c,1], Paivo Kinnunen [a,*]

[a] *Fibre and Particle Engineering Research Unit, University of Oulu, Oulu, Finland*
[b] *Laboratory for Concrete & Asphalt, Empa, 8600 Dübendorf, Switzerland*
[c] *Department of Materials Science and Engineering, University of Sheffield, Sir Robert Hadfield Building, Mappin Street, Sheffield S1 3JD, United Kingdom*

ARTICLE INFO

ABSTRACT

Hydrated magnesium silicate materials are promising binding materials for applications as alternative cementitious materials and may offer a lower carbon footprint than conventional binders if carbon-free feedstocks are used. The reaction of reactive MgO with silica sources yields magnesium silicate hydrate (M-S-H) phases. These M-S-H phases have layered silicate structure and are stable from pH 8 to 12; thus, M-S-H phases are of interest for applications requiring low-pH binders, such as radioactive waste management and encapsulation. Reactive Mg-cements have been extensively studied in the past 100 years, yet the literature does not offer a dedicated review of M-S-H materials. This review provides a critical analysis of the current knowledge on M-S-H-based binders, discussing the main variables involved in M-S-H synthesis, the structure and characterization of these phases, thermodynamic parameters, stability, as well as the mechanical properties and potential applications of the resulting binders.

1. Introduction

Magnesium silicate hydrate (M-S-H) based binders are gaining considerable attention due to their attractive engineering properties as low-pH binders for applications where usual construction materials cannot be used (e.g. waste encapsulation of radioactive materials) [1–6]. Currently, M-S-H materials are produced mainly from MgO obtained through the calcination of magnesite ($MgCO_3$); thus, displaying high carbon footprint. However, M-S-H binders, based on reactive magnesia and silica sources, may also be prepared using widely available low-carbon MgO precursors, thereby making them more environmentally friendly. Indeed, the utilization of MgO-based precursors from abundant non-carbonate sources obtained from 1) concentrated brines [7–15], or 2) extracted from magnesium-silicate minerals such as ultramafic rocks (e.g., olivine and serpentine [16–19]) and inorganic waste-streams (e.g., mine tailings and steel slags [20–22]) could lead to a potential breakthrough in the field of M-S-H binders. That would enable low-carbon M-S-H material production and consequently, indirectly reduce the CO_2 emissions associated to the production of the current calcium-based cements (Portland cement and derived products).

The concept of M-S-H binders dates from >100 years ago [20]. One of the earliest reports of the M-S-H binders was published in 1899 by Cummings [23], who claimed the invention of a new hydraulic cement through calcination and pulverization of magnesium silicate rocks and lime. During the period 1890–1920, there were several innovations toward the development of M-S-H-based binders, which were produced mainly by adding silicate sources to magnesium-containing precursors such as magnesium oxychloride cements [24,25], asbestos [26], talc [27], and others. Since the 1950s, many studies have reported the formation of M-S-H phases in hydrated Portland cement (PC) due to exposure to sea water or $MgSO_4$ [28–32] from the reaction of silica gel in degraded (decalcified) cement paste with magnesium salts from the surroundings [28]. The formation of M-S-H phases has been reported in many other environments, including glass alteration [33], carbonate successions [34], and the interaction zone between clayey rocks and cement [35,36]. Studies on the M-S-H phases received a more systematic dimension in the 21st century when M-S-H phases were synthetically prepared from mixtures containing pure sources of silica and magnesia,

---

allowing better analysis of the structure and properties. Notable works in this direction have been published by Brew [4], Szczerba [37], Zhang [38], Walling [5], Nied [39], Roosz [40] and Bernard [41,42].

Depending on the synthesis parameters, M-S-H binders exhibit good to excellent properties of high strength development, low pH, and thermal properties. These properties increased the potential application of M-S-H binders in different fields, including radioactive waste disposal [43], clay backfilling as stabilizing cement [44], stabilization immobilization of hazardous wastes and heavy metals in construction materials [45,46], 3D printing [47], CO_2 capturing [48], as adsorbent [49] and also for refractory castable manufacturing [50,51]. However, more efforts need to be deployed to understand better the long-term performance of M-S-H binders and their conformity with the standards in the construction field and enable their usage on a large scale in different applications.

The current review compiles the information of a total of 171 former studies selected according to the relevance, coherence and suitability of the observed results. It is offered here a critical analysis of the M-S-H phases and M-S-H binders, considering variable aspects of the synthesis of M-S-H phases, such as the type of precursor, influence of synthesis conditions, and kinetics of the M-S-H formation. Detailed aspects of the M-S-H structure and its characterization are also discussed, expanding the analyses to the mechanical and durability properties of the material. A section has been devoted to thermodynamic modelling and stability aspects of M-S-H phases. The review also includes potential applications as well as the limitations of M-S-H binders.

2. Formation of M-S-H binders

2.1. Precursors

The most common precursors of M-S-H phases are MgO and silica fume (SF) (also known as microsilica (MS)). Table 1 (in the appendix) summarizes the main precursors for precipitating M-S-H phases via synthetic routes employing suspensions, pastes, or mortars. The characteristics of the MgO (calcination temperature) and the silica source (amorphicity and surface area) can have a significant impact on the formation of M-S-H [52]: MgO decarbonated at low temperatures (light-burnt: ~ 700–1000 °C, relative to other temperatures used for production of MgO as hard-burnt (1000–1500 °C), dead-burnt (1500–2000 °C), and fused (>2800 °C) has higher surface area [53] and hence, it leads to higher rate of M-S-H formation. In contrast, higher amorphicity and surface area of the silica source improve the silica dissolution, enhancing the formation of M-S-H [52,54].

Brucite ($Mg(OH)_2$) is also, but less commonly, utilized as a raw material for producing M-S-H binders [5,55]; for example, Walling et al. studied the formation of M-S-H binders from $Mg(OH)_2$ and SiO_2 using sodium hexametaphosphate (SHMP) as a dispersant [5]. $Mg(OH)_2$ was reported to be fully consumed after 28 days of curing, reacting into M-S-H pastes. However, the reported compressive strengths of 2–3 MPa are significantly lower than the average compressive strength of M-S-H binders prepared using MgO. One possible reason for this may be the high water-to-binder ratio used in these studies, which affects the porosity of the materials, but was required (even with an added dispersant) to obtain a workable paste from the high-volume fraction of the plate-shaped $Mg(OH)_2$ particles and high surface-area silica. M-S-H precursors can also be produced from a single feedstock, as shown in the work of Scott et al., where the authors recovered pure MgO and SiO_2 from olivine and used them as precursors to synthesize M-S-H binders [21]. The recovered SiO_2 showed higher reactivity than commercial SF due to its higher specific surface area.

The source of silicate precursor is often silica fume (SF). Recently, silica fume was also used to ensure a homogenous system and avoid the agglomeration of SF [56]. The silicate precursor can be extracted from other low-cost precursors such as metakaolin, fly ash, rice husk ash (RHA), waste glass, slags, clays, and others [21,52,57–60]. Fly ash

usually shows low reactivity for M-S-H formation [22,61], as the pH of most M-S-H-forming mixtures is not sufficiently high to drive significant fly ash glass dissolution [62]. Sonat and Unluer compared the potential of two forms of RHA (crystalline and amorphous) as silicate precursors for preparing M-S-H binders [58]. The sample with crystalline RHA presented the lowest strength due to the low reactivity of these phases. When Ca-rich precursors (e.g., steel slags) are employed as silicate sources, the CaO content (Ca/Mg molar ratio > 0.1) can reduce the effectiveness of M-S-H formation, possibly due to the presence of Ca^{2+} species leading to the formation of C-S-H and eventually inhibiting the formation of M-S-H phases [63]. M-S-H can also be formed from metakaolin sources [57]. The M-S-H binder produced using metakaolin was reported to have higher mechanical strength than the M-S-H binder prepared using SF, due to the additional formation of hydrotalcite ([$Mg_{1-x}Al_xOH$][OH, ½CO_3]·mH_2O), which densified the M-S-H microstructure [64].

2.2. Admixtures

Admixtures are used for multiple purposes in concrete production as they offer an essential lever to modify cement hydration kinetics and enable much lower water-to-binder ratios to reach the same workability. However, to date, only a few studies investigated the effect of admixtures on M-S-H formation [1,5,38,44,55,60,65–70], and a knowledge gap remains [70] Thus, systematic studies on the effects of different admixtures on M-S-H formation are needed to address this gap in the open literature. The admixtures used for Ca-based systems do not directly transfer to Mg-based cements, and further developments are still required to achieve well-functioning additives for Mg-based cements.

Sodium hexametaphosphate (SHMP) additives reduce the water demand and improved the fluidity of the M-S-H paste [38], due to the coating of the cement particles, consequently leading to negative charge particles [71]. The addition of 1 wt% SHMP to an M-S-H binder made from MgO and SF with Mg/Si = 1 in the presence of SHMP [1] reduced the w/b ratio to 0.4 (from 0.9 without SHMP), similar to the standard w/b ratio used for PC. SHMP can also be used to synthesize M-S-H from $Mg(OH)_2$ and SF [5], Fig. 1 shows how the SHMP can improve the mini-slump value while decreasing the w/b ratios. Generally, introducing SHMP considerably improves the workability of M-S-H samples and yields higher compressive strengths due to lower porosity [1,5,65]. Adding >2 wt% of SHMP was found to retard M-S-H formation, although it increased the compressive strength of the hardened material [5]. The presence of phosphate at moderate concentrations may also enhance the kinetics of M-S-H formation as it suppresses the brucite formation [38,66] due to magnesium-phosphate complexation in solution [44]. However, the final fate of the small amount of phosphate added in this type of cement has not been fully determined, and the phosphate's role in the mechanical or durability properties of the cements needs further investigation.

Using a polycarboxylate-based superplasticizer (Viscocrete-5-555) significantly reduced the water demand of an M-S-H binder produced from 40 % MgO and 60 % SF [67]. The optimal loading of superplasticizer (Viscocrete-5-555) was found to be 1.0 to 1.5 % (based on binder), leading to a 41 % reduction in water demand.

Adding $NaHCO_3$/Na_2CO_3 is reported to accelerate the formation of M-S-H gel during the reaction between $Mg(OH)_2$ and SF [55,68]. The addition of $NaHCO_3$ led to an increased dissolution rate of silica (by buffering the pH at ca. 10.2); and improved the fluidity of the paste, enabling the synthesis of M-S-H at low w/b ratio without the need for any dispersants. Adding $NaHCO_3$/Na_2CO_3 solution enhanced the reaction between $Mg(OH)_2$ and MS, accelerating the M-S-H gel formation. The extent of the reaction was most significant when the added Na_2CO_3 solution was near saturation. The authors attributed this to the effect of pH (which controls the dissolution of brucite and silica) as well as to the presence of carbonate ions [68]. It was also noted that the presence of carbonate ions in the system induced the formation of hydromagnesite
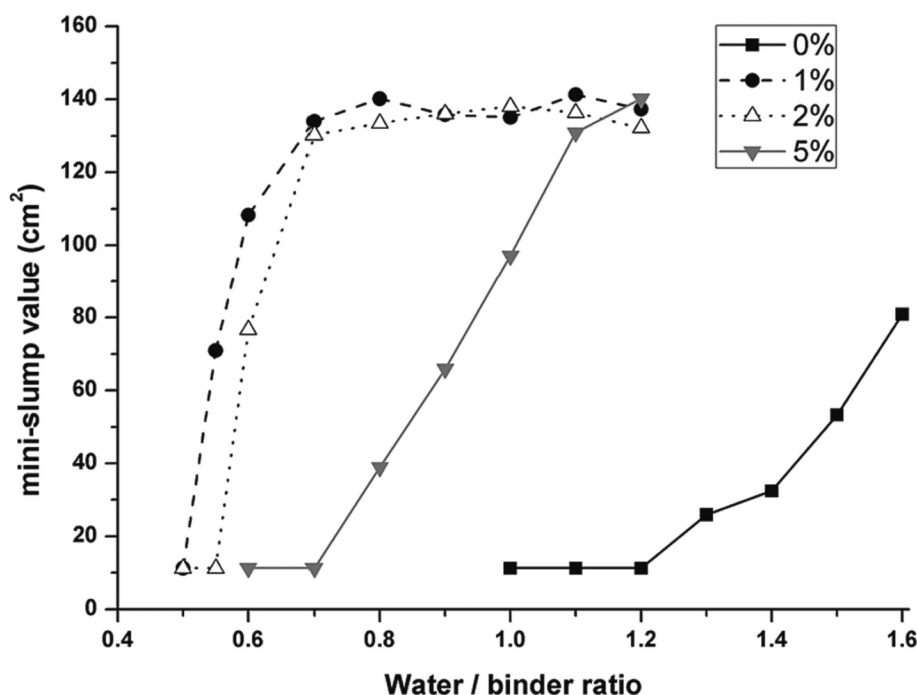
Fig. 1. Mini-slump value as a function of w/b ratio for M-S-H samples produced from Mg(OH)$_2$ and SiO$_2$ with 0–5 wt% SHMP. A measurement of 11.3 cm^2 indicates no slump. Reproduced from [5], CC-BY license, with permission from the Royal Society of Chemistry.

(hydrated magnesium carbonate) as a competitive phase [55]. M-S-H phases form faster in the presence of carbonates, which complexes with the dissolved Mg, thus increasing the Mg concentration in solution and destabilizing brucite.

Interestingly, hydromagnesite seeds increased the degree of hydration, enhancing M-S-H formation and yielding better microstructure development and mechanical performance [69], potentially related to the dissolved carbonates, which would increase the Mg concentration in the solution due to the complexation of carbonates and magnesium.

The addition of MgCO$_3$ to M-S-H binders prepared from MgO and silica fume did not show significant changes [60]. However, the same addition to MgO combined with calcined clay or metakaolin increased the early compressive strength in 150–200 % in blends with calcined clay or metakaolin implying an increment in performance of blends containing reactive alumina due to MgCO$_3$ addition [60]. Considering the long-term performance: MgO-metakaolin blends with both 4 wt% and 12 wt% MgCO$_3$ showed higher early compressive strengths (3 and 7 days strengths) compared to MgO-metakaolin blend without MgCO$_3$. However, the performance of the blend with 12 wt% MgCO$_3$ dropped over time. After 90 days, the blend with 4 wt% MgCO$_3$ had significantly higher compressive strength than the one without MgCO$_3$, while the blend with 12 wt% MgCO$_3$ had significantly lower compressive strength than the blend without MgCO$_3$. That was justified by the excess of hydrotalcite formed in the blend with 12 wt% MgCO$_3$, which creates internal stresses related to the expansion promoted by the volume of the phase, thereby leading to cracks, higher porosity, and lower strength.

The current progress on the uses of admixtures indicates high potential for tunning the final properties of M-S-H binders according to the targeted applications. However, further developments are needed to evaluate a broader range of possible additives and to determine the long-term effects of potential admixtures.

2.3. Water demand

The w/b ratio is known to have a critical influence on the workability and the porosity of cementitious materials, and so is an essential parameter for tuning the M-S-H phases for construction applications [1].

Although higher w/b ratios lead to improved paste workability, this also tends to lower mechanical strength due to higher porosity in the hardened material. It was reported a 40–50 % drop in the compressive strength of the M-S-H product when the w/b ratio increased from 0.4 to 0.8 [1]. As discussed above, dispersants like sodium hexametaphosphate can be used to reduce the w/b ratio of M-S-H paste, leading to improved workability and higher strength [38]. M-S-H binders generally have higher water demand than PC binders due to the high surface area of solid precursors, especially silica fume. The water demand for silica fume-based materials is reported to be almost seven times higher than that of PC [72]. Depending on the raw materials, the minimum water demand of silica fume-based materials is almost three times that of PC [73]. While the water demand is higher in magnesium-silicate binders due to the small particle size of the starting materials, it should be noted that M-S-H phases (hence binders based on M-S-H) bind about 25–30 wt % water (physical water, and hydroxyl groups bonded to Si and Mg [42]), slightly higher than in the PC system (20–25 wt% water [74]).

2.4. General mechanisms and kinetics of M-S-H formation

The simplest system for understanding the kinetics of M-S-H formation involves the precipitation of M-S-H phases in suspensions containing magnesium oxide and silica fume. Hence, this section focuses on these reactional systems. During the first day, MgO dissolves rapidly, while silica fume is slowly dissolved. That leads to brucite precipitation and pre-nucleation of M-S-H clusters in the first 3 days. The M-S-H phases are formed gradually afterward (while the brucite contents are reduced after 7 days) until all SF or brucite are fully consumed [75]. The general mechanism of M-S-H precipitation in such systems is described to occur in three main steps: (i) The hydration of MgO to form brucite, which is affected by the content of dissolved silicates [76] due to the kinetic inhibitory effect of silicate on the formation of M-S-H clusters [37,41] (ii) Brucite (Mg(OH)$_2$) reacts with dissolved silica to form a transient M-S-H phase with a lower degree of organization than the final product [41]; and, (iii) the later replacement of this transitional phase by the final M-S-H phase with a more ordered structure and potentially a different Mg/Si ratio (which is dependent on the Mg/Si ratio of the

precursor) [41]. The rate-determining step in M-S-H formation is the dissolution of brucite, which controls the Mg concentrations in the system [41]. M-S-H formation seems to follow Ostwald's step rule, meaning that the phase with the lower kinetic barrier forms first.

The formation rate of M-S-H phases at 20 °C through precipitation from aqueous suspensions in an inert atmosphere can be estimated by calculating the contents of unreacted brucite (e.g. TGA analysis) and the unreacted silica content (e.g. ^{29}Si MAS NMR analyses) as shown in Fig. 2 [41]. After one week, the solutions reached equilibrium with respect to the contents of amorphous silica, and M-S-H phases formed, usually presenting a Mg/Si ratio ranging from 0.67 to 1.00. The unreacted silica content of the 3-month-aged sample with Mg/Si ratio of 0.8 was approximately 16 % and dropped to ca. 4 % after 12 months. In the sample with a Mg/Si ratio of 1, the unreacted silica dropped from 6 % after three months to 0 % (i.e. full reaction of SF) after twelve months. A noticeable amount of brucite remained in all samples after three months, linearly proportional to the initial MgO contents. After six months of curing, brucite has been observed only in the samples with Mg/Si > 1.1. The 24-month-aged samples showed residual brucite only in those with Mg/Si > 1.2. Although brucite is observed in every M-S-H sample in short-term experiments (up to 3 months of curing time), the solutions exhibited undersaturation with respect to brucite after 2 days of curing, indicating that dissolution of brucite is the rate-determining step as concluded by the authors [41]. Additionally, if the solubility of brucite is close to the solubility of M-S-H, it would lead to a low degree of supersaturation and, therefore slow precipitation rates. The proximate cause for the slow dissolution rate of brucite would not, therefore, be inherent to the ability of brucite to dissolve but would also depend on the precipitation rate of M-S-H.

Regardless of the Mg/Si ratio of the sample, the initial transient M-S-H phases formed have Mg/Si ratios between 0.9 and 1.1. However, when equilibrium is supposedly reached (after 2 years), the M-S-H phases can have slightly different compositions, exhibiting a Mg/Si ratio between 0.8 and 1.3. Longer equilibration times (3.3 years) are reported to initiate a slow ripening of M-S-H phases, related to Ostwald's step rule, resulting in their lower solubility. The slow kinetic of the system is considered to be affected by several factors such as temperature, Mg/Si ratios, properties of the employed precursors, w/b ratio, and pH [41].

The increased curing temperature of the samples are also known to fasten the formation of M-S-H [37,41]. However, the obtained M-S-H phases have slightly lower thermodynamic stability [41], although high-temperature curing has also been reported to improve the local ordering of M-S-H gels [77]. The specific surface area of M-S-H is reported to be unaffected by the curing temperature but decreases with curing time, implying larger particle formation [42]. Extended curing times were observed to lead to higher polymerization degrees [41] and improved mechanical properties [1].

The pH of the pore solution significantly impacts the formation of the M-S-H phases: during the first 7 days, the pH is higher than 10.5, and brucite is the main reaction product. After 7 days, the pH is lower than 10.5, and M-S-H gels are formed with gradually increasing proportions. The optimum pH was found to be 10.5, which led to the highest concentration of dissolved Mg and Si (see Fig. 3a), thereby leading to the highest formation of M-S-H phases [75]. A schematic illustration of M-S-H formation in pastes is shown in Fig. 3.

Adding Na_2SiO_3 solution to magnesium chloride solution raises the pH from 6 to 10.7 in the pre-nucleation step of M-S-H formation [78]. M-S-H nucleation occurs under a critical concentration of Mg^{2+} and silicate species, together with the maximum pH value of the pore solution. After the onset of nucleation, the pH reaches a quasi-constant value, indicating the reaction with the silicate species and the incorporation of the hydroxyl ions into the M-S-H layers [78]. The addition of Cr^{3+} has a catalytic effect on the nucleation step [78]. Other cations such as Li^+, Ba^{2+}, Cs^+, Fe^{3+}, Co^{2+}, Ni^{2+}, Cu^+, Zn^{2+}, Pb^{2+} and Al^{3+} do not promote remarkable kinetic changes [78]. Later, Cr, Co, and Fe showed a kinetically inhibitory effect in the growth period. All investigated additive cations in this study, strongly affected the structure and morphology of the precipitated M-S-H. Hence, secondary metals could be incorporated into the M-S-H structure via different mechanisms controlled by ion association properties and the secondary phase solubility [3].

The kinetic of M-S-H formation is also influenced by other factors such as reactivity of MgO, silica source, hydration agents, Mg/Si ratio, curing temperature, etc. [5,52,57,79].

2.5. Molar composition

As detailed in the previous section, one of the most important factors controlling M-S-H formation is the concentration of Mg and Si in the solution. The Mg/Si ratio in the reacting system has a critical influence on the pH and, consequently, on the dissolution of precursors and on the
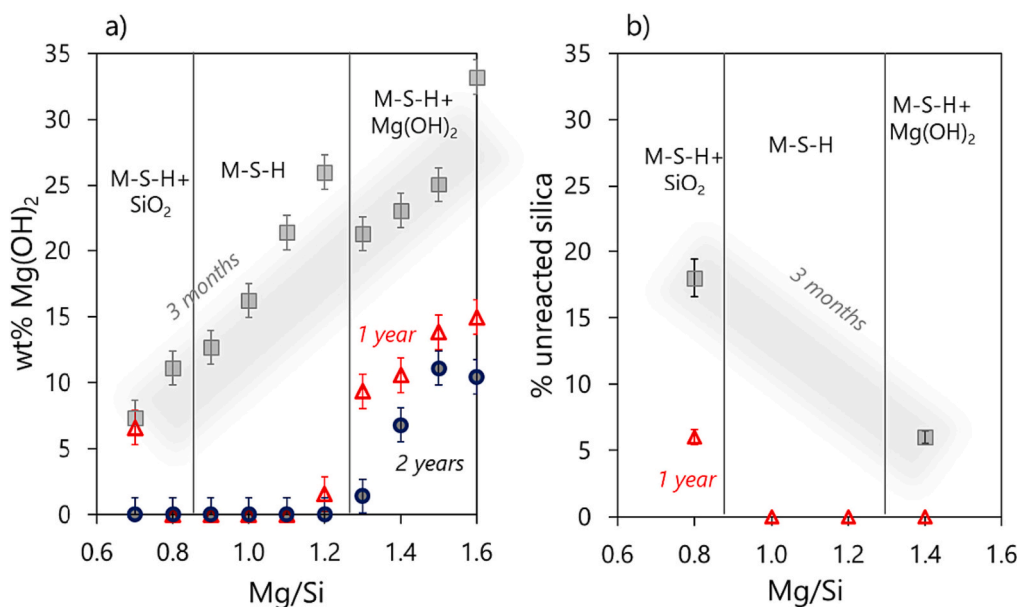

Fig. 2. Amount of (a) unreacted brucite (calculated by TGA analysis) and (B) unreacted silica (estimated from ^{29}Si MAS NMR analysis) present in M-S-H phases cured at 20 °C as function of Mg/Si and time, adapted from [41].
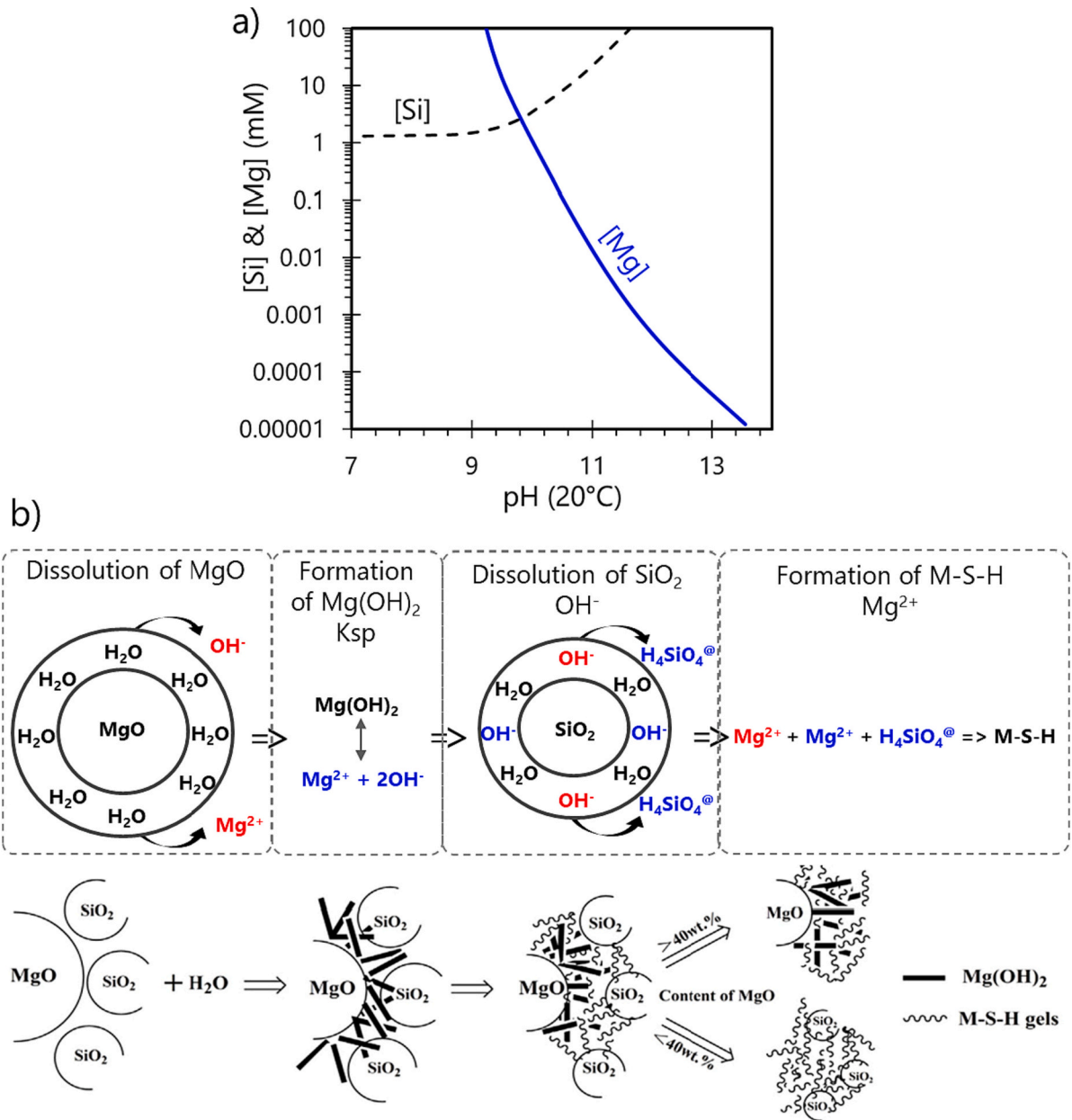
Fig. 3. (a) Solubility of amorphous silica and brucite following the thermodynamic data given in [41]. (b) A schematic illustration of M-S-H formation in pastes, adapted from [75].

structure of the precipitated M-S-H phase (Section 3.1). Nied et al. have investigated variations in the bulk Mg/Si ratio (from 0.7 to 1.5), observing the part of the silicate precursors remains unreacted at lower Mg/Si ratios. In comparison, residual brucite is notable at higher Mg/Si ratios [39]. Based on these observations, those authors identified the lower and upper limits of the Mg/Si molar ratio in M-S-H cured for 1 year to be around 0.8 and 1.3, respectively [39]. An increase in Mg/Si ratio leads to higher total coordinated water and lower specific surface area of the precipitated M-S-H phase [39]. Recent studies have demonstrated that Na_2CO_3 addition enabled the precipitation of M-S-H phases at an Mg/Si ratio of 1.5 [80].

Several impurities (e.g., calcium, aluminium, and iron) must be considered when industrial side streams are employed as feedstocks for M-S-H precipitation. The presence of calcium can lead to the formation of C-S-H, which may form a competitive phase to M-S-H [81]. The absence of any extended solid solution between M-S-H and C-S-H is reportedly due to the difference in the ionic radii of Mg^{2+} and Ca^{2+} [81].

Using metakaolin in addition of MgO, silica fume showed the isomorphic replacement of Al^{3+} in the Si^{4+} and Mg^{2+} sites, forming an M-A-S-H phase [82]. The M-A-S-H phase has been shown to be comparable to M-S-H in terms of limited coherent size and silicate polymerization. The aluminium presents in the precursors as metakaolin is also reported to form hydrotalcite-group phases, mostly leading to a densified micro-structure and higher mechanical strength of the binder compared to aluminium free systems [57,64]. The formation of an iron-magnesium-silicate-hydrate (F-M-S-H) phase was also observed in the interaction of alkaline seepage (pH > 11) with sediments derived from serpentinized ultramafic rocks, finding that iron also undergoes isomorphic replacement into the M-S-H structure [83].

When an M-S-H phase is obtained from the exposure of hydrated PC to seawater, the Mg/Si ratio seems to be able to span a broader range, from 0.5 to 2.0 [84,85], although the observed Mg/Si in synthetic systems is from 0.8 to 1.5 [39,80]. Fig. 4 shows the Mg(+Ca) - Si - Al(+Fe) molal ternary plots based on the composition of the different M-S-H
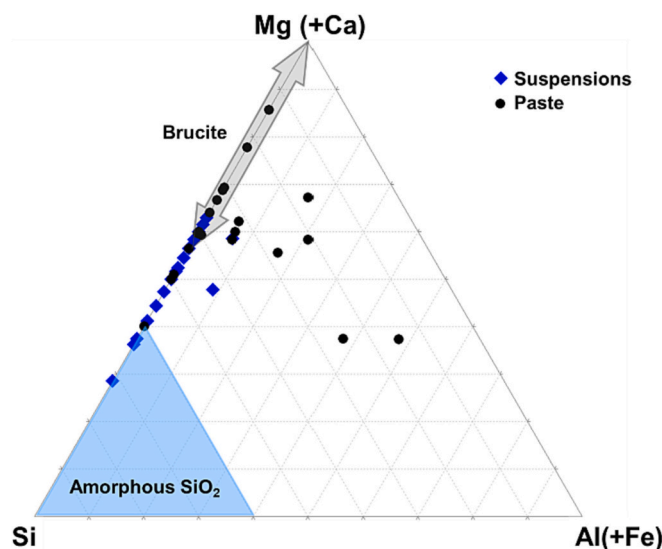
Fig. 4. Mg(+Ca) - Si - Al(+Fe) molal ternary plots based on the composition of the different M-S-H mixes found in literature based on Table 1 (Appendix).

mixes found in literature based on Table 1 (Appendix). Overall, the following observations can be made: Si mole fraction range in suspensions is higher than that in pastes (3.7–7.2 vs 1.4–6.0); Mg(+Ca) mole fraction range in suspensions is lower than that in pastes (2.8–6.3 vs 3.8–8.6); Al(+Fe) mole fraction range in suspensions are lower than that in pastes (0.0–0.8 vs 0.0–4.8).

3. Characterization and structure of M-S-H phases

3.1. Chemical and crystallographic structure

M-S-H materials were formerly considered similar to C-S-H phases, mainly due to their identification as phases formed during the degradation of PC-based cements in environments of high salinity (e.g. seawater). The current developments in M-S-H research provide essential information while elucidating the M-S-H structure; however, in-depth information is not yet defined. M-S-H phases are considered as complex composite-like systems of multiple amorphous hydrate magnesium silicate phases, which can resemble different families of clay minerals (depending on the Mg/Si ratio) [86]. In the current section, we will describe the well-known structural features of M-S-H phases, which were elucidated from different techniques found in literature, and the following section will highlight the experimental findings supporting the current knowledge on the topic.

The XRD characterization of M-S-H phases with varying Mg/Si ratios is shown in Fig. 5a [39]. The broad reflections at ca. 19.7°, 26.7°, 35.0°, and 59.9° 2θ are present in all samples. The positions of the reflections are close to those of talc, which exhibits reflections at 9.5° (001), 19.5° (110), 28.6° (003), 36.1° (131) and 60.5° (060) in 2θ [87,88]. The reflections could also be compared to those of antigorite, lizardite, or clay-like structures such as stevensite and hectorite, however, they are observed at higher displacement of the XRD reflection in the (001) direction of the M-S-H phases when compared with analogous clay minerals. Interestingly, when clay minerals undergo exfoliation treatments, the main observed effect is the increasing disorder along the (001) direction [89], which makes the XRD patterns of exfoliated clays similar to the analogous M-S-H material. Indeed, M-S-H reflections at ca. 7° - 9° 2θ are assigned to the interlayer space ((001) reflection), and the minimal coherent regions can cause shifting of this reflection [42]; thus, estimating the interlayer distance based on XRD analyses can produce overestimated values [40]. The characteristic broad (00l) reflections (in Fig. 5a) imply that the M-S-H crystallites are larger in the other (hkl) directions, evidencing the plate-like morphology. Moreover, the wide peaks of all (hkl) reflections raise uncertainty about the structural arrangement of M-S-H: it may mean that the layered silicates are formed with nanocrystalline, or amorphous structure in the M-S-H materials.
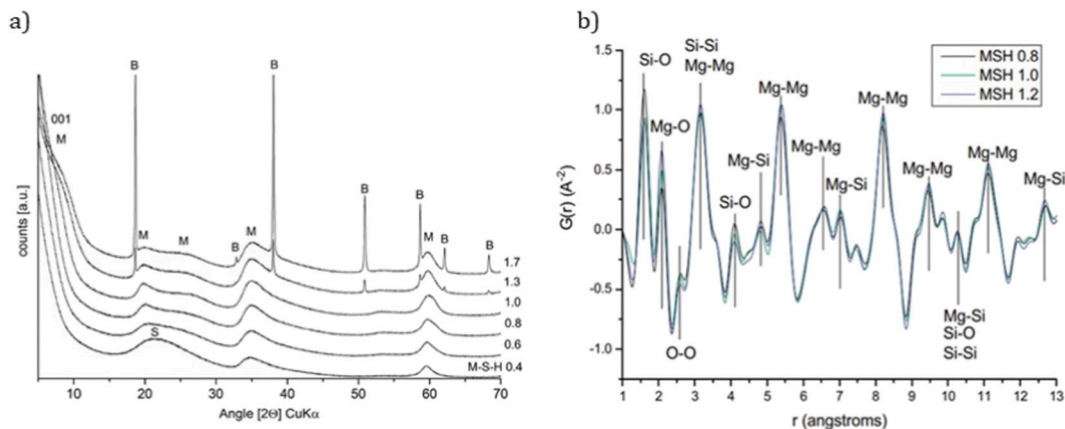

Fig. 5. a) XRD analysis for M-S-H (cured at 20 °C for 1 year) with varying Mg/Si ratio (M: M-S-H, B: brucite, S: unreacted SiO$_2$) reproduced from [39]. b) X-ray pair distribution function (PDF) data for M-S-H (cured at 20 °C for 1 year), reproduced from [42]. All data shown are for synthetic sample sets of varying Mg/Si ratios, denoted "M-S-H x" where x is the Mg/Si ratio.

For this reason, advanced techniques such as small angle X-ray scattering (SAXS) or pair distribution function (PDF) analysis are important to distinguish these features. Roosz et al. attributed the asymmetric nature (intensity rises steeply on the low-angle side and falls slowly on the high-angle side) of some bands to the lamellar and turbostatic structural disordering of M-S-H [40].

The results of the X-ray pair distribution function (PDF) analysis of M-S-H samples (Fig. 5b) are cohesively similar regardless of the Mg/Si ratio. The peaks are attributed to Mg—O ($r = 2.09$ Å) and Mg—Mg (3.13 Å, 5.36 Å, 8.21 Å) distances in the same layer, as well as Si—O (1.61 Å) and Si—Si (3.20 Å) distances in the silicate layer, in agreement with the idealized layered M-S-H structure. As the Mg/Si ratio increases, the intensity of the Mg—O peak (2.1 Å) increases, while that of the Si—O peak (1.6 Å) decreases, indicating an increase in MgO sites and depletion of SiO_2. Experimental uncertainties probably cause minor variations observed in the peak maxima positions. The PDF of M-S-H was compared to that of sepiolite, talc, antigorite, and brucite; the crystalline minerals present coherent lengths higher than 20 Å, while the coherence length of M-S-H (Mg/Si = 0.8) was observed around 12 Å. Thus, the low coherent length of M-S-H can be attributed to its nano-sized particles, while the layered structure is an essential and characteristic feature [42].

Those evidence indicates the structure of M-S-H phases to be comparable to that of minerals belonging to the serpentine and talc families of clay minerals, with similar chemical environments and structures [86]. Therefore, M-S-H materials show intermediate features between the T:O and T:O:T types of clay minerals (Fig. 6), having tetrahedral (T) layers of silicon oxides intercalated with octahedral (O) layers of $M^nO_x(OH)_y$, where M is the central cation (e.g. Mg^{2+}, Al^{3+}), $n = 1$ to 3, and $x + y = 8$. The different types of clay minerals are categorized according to how these polymeric layers connect to each other. The polymeric oxide sheets are separated by an interlayer space, the size of which is directly related to the electrostatic interactions between the layers: the isomorphic replacements occurring in the tetrahedral and/or octahedral layers determines the total charge density of the layers, also defining the interlayer space. Both types of clay minerals have phases formed with dioctahedral or trioctahedral units (having either two or three octahedral units for each tetrahedral unit). In general, T:O type clays have smaller interlayer spaces than the T:O:T type, which is an important feature that determines the properties and usages of these clay mineral-based materials; the contents and sizes of chemisorbed guest species in particular, are determined by the size of the interlayer space [90].

The M-S-H morphology of M-S-H materials (Mg/Si = 1.2) were identified with TEM imaging as nanosized fibrillar particles (Fig. 7a) with a crystallite size of around 100 to 150 nm; however, magnified images (Fig. 7b) reveal lamellar and nanometric structures. The average number of packed layers is usually around 5. The bending of sheets is also evident, especially in the zoomed highlight [40].

The ^{29}Si MAS NMR characterization of orthosilicate-based materials can probe the degree of polymerization of the tetrahedral layers, denoted as Q^n, representing a silicate tetrahedron having n shared oxygen atoms ($0 \leq n \leq 4$). The chemical shifts of tetrahedral silicate units are typically identified from −60 to −140 ppm. Increasing polymerization degree of the Q^n building units is followed by a characteristic upfield movement (to lower frequency / more negative chemical shift). Clay minerals usually display two main signals in the ^{29}Si MAS NMR spectra: those associated with the Q^2 ($Si(OSi)_2(OH)_2$) at ca. -74 to −92 ppm, and Q^3 ($Si(OSi)_3OH$) sites at ca. -93 to −101 ppm. M-S-H–based materials will also often have an additional peak corresponding to Q^4 ($Si(OSi)_4$) sites, due to developing units in the silicates framework, i.e.,
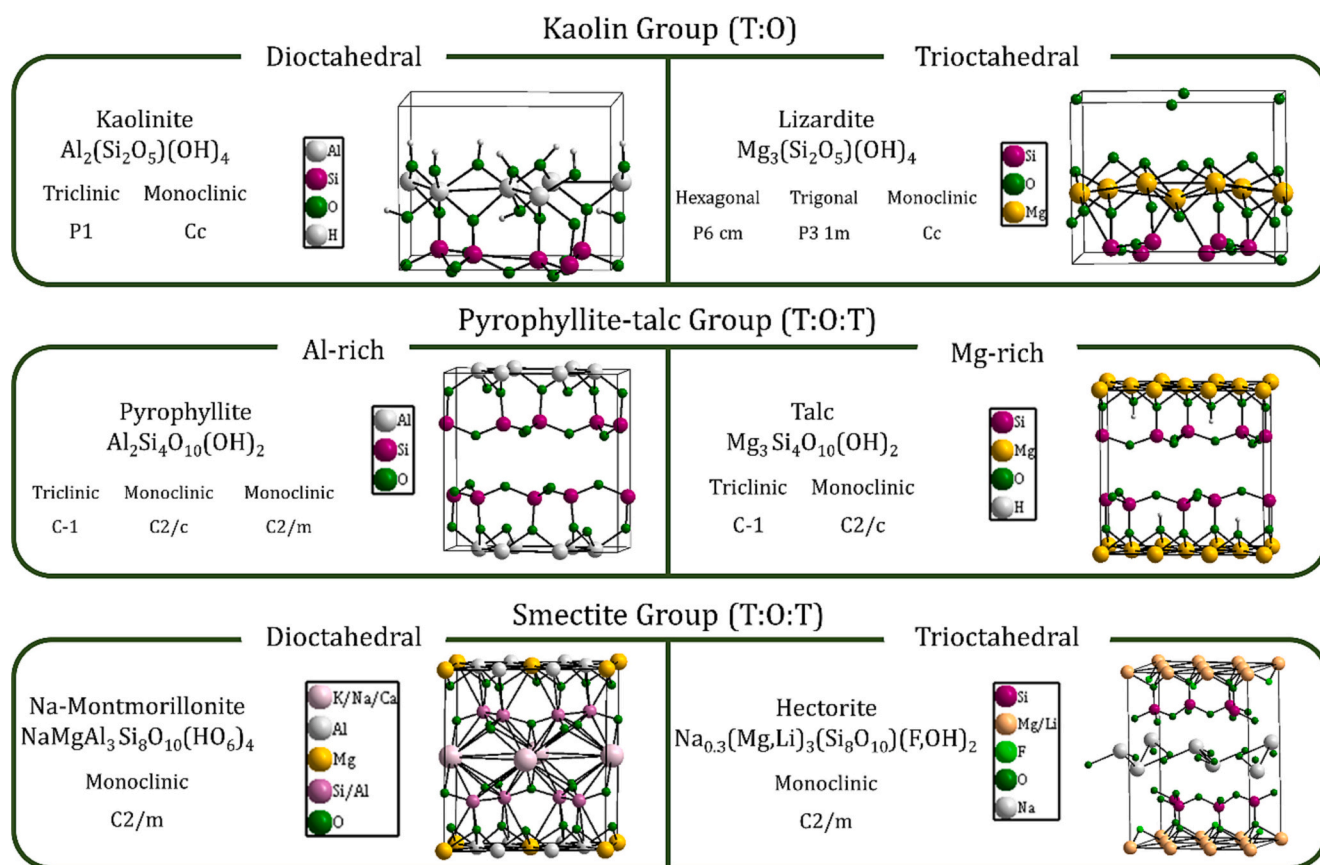

Fig. 6. Structures of clay minerals belonging to T:O type (kaolin group) and T:O:T type (pyrophyllite-talc and smectite groups), showing also typical dioctrahedral and trioctahedral minerals of these groups. Crystal structures were drawn with Diamond crystal impact software, version 4.6.4. The crystallographic information (.cif files) were obtained from the PDF4+ software (version 4.22.02, 2022). The frames around the structures represent the unit cell.
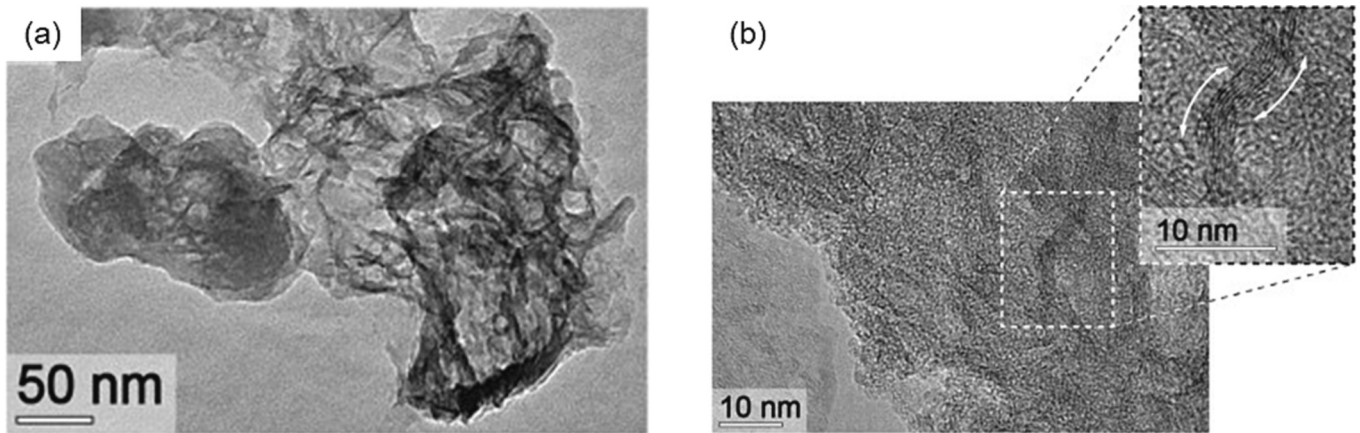
Fig. 7. TEM image of M-S-H with Mg/Si ratio of 1.2 at (a) low magnification (b) high magnification (with zoomed portion showing bending of particle), reproduced from [40].

Table 2
The chemical shift values and the attribution of various Q^n species identified in the ^{29}Si MAS NMR spectra of the M-S-H phases; data are all compiled from papers using spectrometers operating at 79.4–79.5 MHz for consistency.

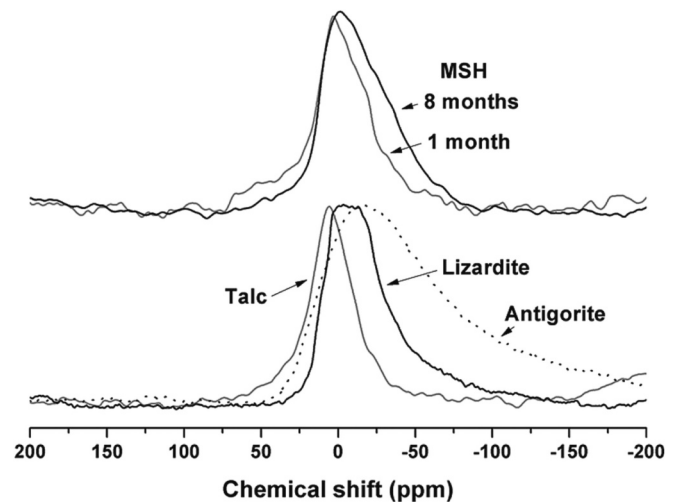| Species	Chemical shift (ppm)	Structural assignment
Q^1	−78.3 [42] −78 [39] −78.9 [40] −81.0 [5]	Silicon vacancy due to breaking of Si sheet/nanocrystallinity [40]
Q^2	−85.4 [39,40] −85.5 [42] −85.2 to −85.5 [94] −86.0 [5]	Similar to Q^2 sites in enstatite [39]; Silicon vacancy due to breaking of Si sheet/nanocrystallinity [40]
Q_a^3	−92.7 [42] −92.3 to −92.7 [94] −92.4 [39] −92.9 to 93.5 [5]	Serpentine group minerals (antigorite/ chrysolite/ lizardite) with T:O structure [39,95]; Consistent with Q^3 peak in chrysotile and antigorite [5]; Near edge of the silicate sheets in the blocks in sepiolite [96–98]
Q_b^3	−94.7 [42] −94.6 [39] −93.4 to −94.5 [94]	Presence of empty Mg site in stevensite [99,100]; High amount of surrounding water in M-S-H, which leads to resonance at −95 ppm as in case of saponite/stevensite/hectorite [86]; Variability of Si-O-Si angles in M-S-H [42]; center or edge of silicate sheets [96–98]
Q_c^3	−96.7 [39] −96.7 [42] −97.7 [5] −98.2 [94]	Talc structure with T:O:T structure [39,40,100,101]; Consistent with Q^3 environment in talc [5]; center or edge of silicate sheets [96–98]
Q^3 (-OH)	−101 [39]	Silica surface sites $(SiO)_3Si^*$-OH of unreacted silica [39]
Q^4	−111 [39] −112 [39]	Fully condensed $(SiO)_4Si^*$ sites of unreacted silica [39]

Fig. 8. ^{25}Mg MAS NMR spectra of M-S-H (Mg/Si = 1.0, cured for 1 and 8 months) and magnesium silicate minerals [5]. Note that the spectrum for antigorite is broadened by the presence of iron.

some amorphous silica excess present in the material [91].

The chemical shift values and the attribution of the Q^n species identified in the ^{29}Si MAS NMR spectra of M-S-H phases are listed in Table 2, which slightly differ from those observed for clay minerals. The ^{29}Si MAS NMR spectra of M-S-H generally exhibit roughly 2/3 Q^3 signals and 1/3 of Q^2 signals [39,40,42]. The Q^3 signals appear at ca. -92 to −97 ppm and include 2 or 3 different Q^3 sites (identified as Q_a^3, Q_b^3, and Q_c^3) [5,39,92]. However, it can be that the ^{29}Si MAS NMR spectra of M-S-H present a significant proportion of Q^3 sites (when compared to Q^1 and Q^2 sites) throughout the curing regime, indicating a higher degree of polymerization of the silicate layer [93]. In this particular study, the M-S-H structure was observed to be very similar to the one of lizardite.

The literature presents relatively few studies on the ^{25}Mg NMR analyses of M-S-H phases [5,39,93] due to two main reasons: 1) ^{25}Mg has a

low natural abundance and low resonance frequency, which requires very high field instruments, and 2) the quadrupolar nature of ^{25}Mg makes the interpretation of the spectra complex [5]. The asymmetric feature is typical for a broad quadrupolar coupling parameter distribution is coherent with the disordered nature of M-S-H. Distinct peaks at −5 ppm and − 52 ppm are not related to M-S-H but rather to unreacted brucite present in the sample. ^{25}Mg MAS NMR spectra of pure M-S-H samples (Mg/Si = 1.0, cured for 1 and 8 months) and magnesium silicate minerals [5] is presented in Fig. 8. The spectrum shifts upfield as the M-S-H sample undergoes curing from 1 to 8 months. The spectrum of the M-S-H sample cured for 8 months resembles lizardite more closely than talc or antigorite, and similar observation has also been made elsewhere [93].

Recent work has also identified via classical molecular dynamics (MD) calculations that the M-S-H phase at Mg/Si $\cong$ 1 can be described by a structure composed of a defective talc-based model or as a mix of amorphous models of talc with modest contents of amorphous lizardite (Fig. 9) [86]. The authors of this study aimed to build a realistic model of M-S-H phases by using lizardite and talc crystals as a basis for their models, modifying their structures to reach Mg/Si = 1 and the Q^n site distributions proposed from previous experimental works. The simulations demonstrated M-S-H binders to have a layered structure resembling lizardite and talc crystals, with water molecules sandwiched
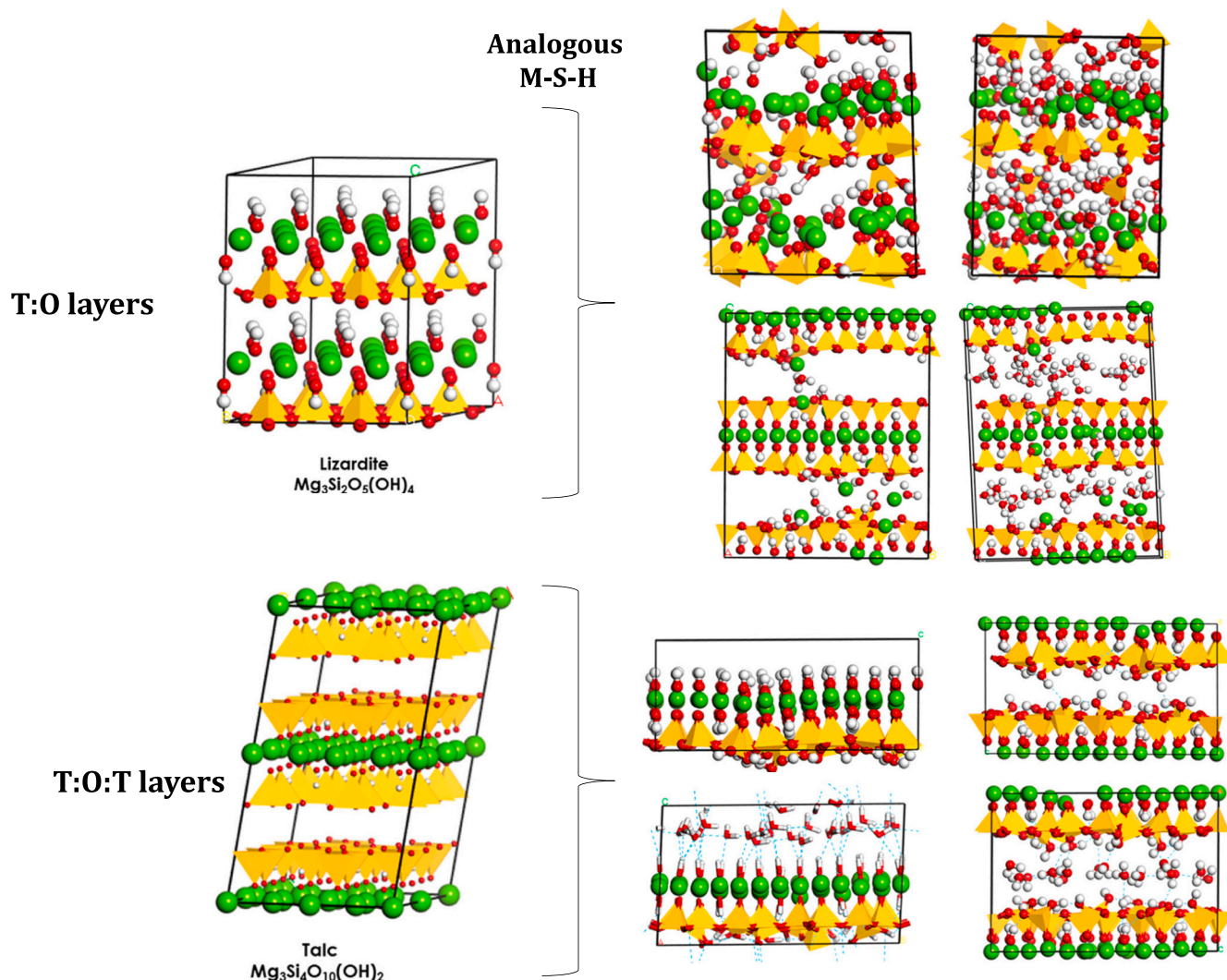
Fig. 9. Snapshots of DFT-optimized structures of lizardite (T:O) and talc (T.O:T) before (left) and after (right) simulating the relaxation of defective talc-like and lizardite-like structures to form M-S-H phases. The tetrahedra shown are silicate units, while green, red, and white balls represent Mg, O, and H atoms, respectively. Adapted with permission from Pedone et al. (J. Phys. Chem. C 2017, 121, 7319–7330) [86]. Copyright © 2017 American Chemical Society. (For interpretation of the references to colour in this figure legend, the reader is referred to the web version of this article.)

between the T:O and T:O:T layers. They also observed that while the Si environments in the models were similar, the talc-based models and the models containing water molecules had a narrower Si-O-Si bond angle distribution than that of the lizardite-based models, denoting a more regular environment. In terms of the Mg environment, 6-fold coordinated Mg atoms with average distances between 2.07 and 2.10 Å in a chemical environment more similar to that of talc than of lizardite are likely to provide ^{25}Mg MAS NMR spectra consistent with the experimental observations of M-S-H phases. Overall, the results of the simulations showed that M-S-H binders share some structural similarities with clay minerals such as talc and lizardite, but also have unique properties due to their disordered layers and variable interlayer spacing, which are determined by the charges of the layers and the consequent amount of intercalated and absorbed water [86].

3.2. Effect of Mg/Si in the M-S-H structure

Consequently, the structure of M-S-H materials has been compared to diverse types of clay minerals, such as sepiolite [77], lizardite [5], talc [39,40], stevensite [39], saponite [40], antigorite [20], chrysotile [20], and hectorite [102]. The partially disordered nature of M-S-H phases can hinder the accuracy of its structural determination, as amorphized phases of clay minerals can have similar structural features (e.g. antigorite, chrysotile, and lizardite), which may lead to ambiguous conclusions in the structural determination of M-S-H phases [20]. Nevertheless, relevant works have implied a direct relationship between the amount of intercalated water in the M-S-H structures and the respective Mg/Si ratio of the M-S-H phase, demonstrating that the structure of M-S-H is highly dependent on the Mg/Si ratio [40,77]. From the point of view of the XRD, little changes could be observed, from diffraction X-ray patterns or PDF. The reflections of M-S-H with low and high Mg/Si ratios slightly differ in terms of the intensity at ~7º and ~ 20º 2θ [40,42].

The ^{29}Si MAS NMR spectrum obtained for an M-S-H phase with Mg/Si = 0.6 is shown in Fig. 10a [39]. An increase in Mg/Si ratio leads to higher proportions of Q^2 species [41], and the aging process decreases the proportion of Q^3_a sites while that of Q^3_b and Q^3_c increased [41]. The Q^3_c can be attributed to silicate sheets with a higher degree of ordering [41], whereas the Q^2 sites may be attributed to edges of the very small coherent silicate regions in M-S-H [40] or the presence of double/triple silicate chains [41]. The ^{29}Si chemical shifts are more negative in the talc structure than in serpentine-type minerals due to the existence of a second SiO_4 layer on the other side of the MgO_6 layer [42]. A higher intensity of Q^3_a (−92.7 ppm) in M-S-H indicates a greater structural
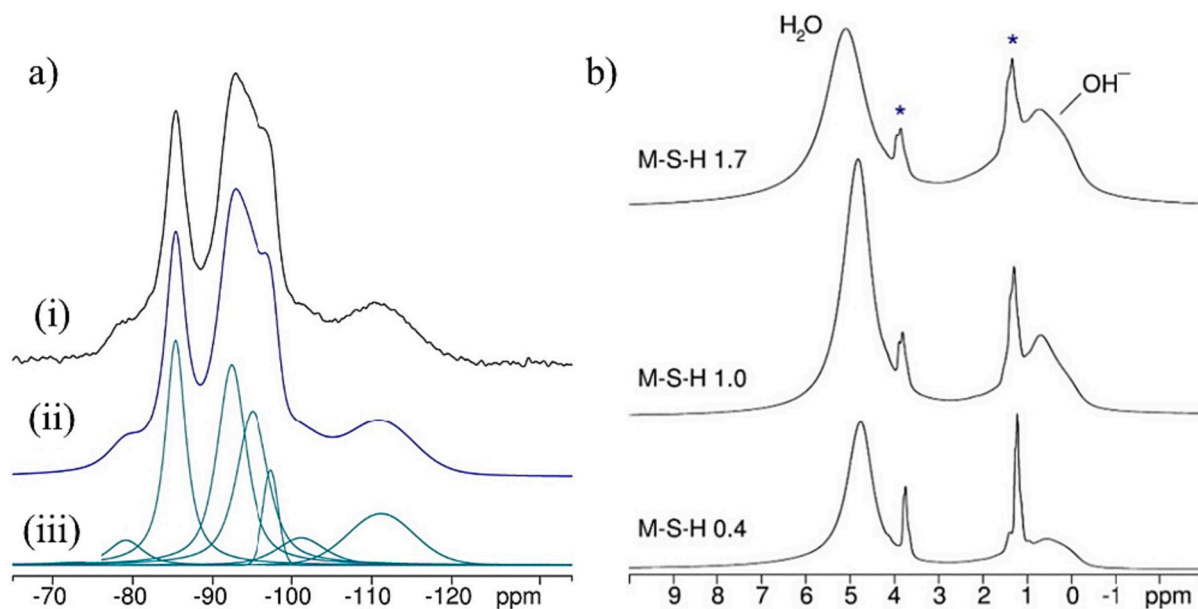
Fig. 10. a) (i) ^{29}Si MAS NMR spectrum of an M-S-H phase with Mg/Si = 0.6, and (ii) the optimum deconvolution, using the peaks shown in part (iii) [39]; b) ^{1}H MAS NMR spectra of M-S-H with varying Mg/Si ratios [39].

Table 3
The main vibrational modes observed in the FTIR analysis of M-S-H phases.

Approximate position of absorption band (cm^{-1})	Vibrational modes	Reference
665	Si—O—Si bending in M-S-H	[39]
800	Si-O-Si stretching of unreacted silica[a]	[5,39,52,69]
870 to 920	Si-O asymmetrical stretching of Q^2 tetrahedra in M-S-H	[39]
875	C-O bending in carbonate ions (weak band)	[39]
885	Si-OH bending in the residual hydrated silica	[5]
950 to 1100[b]	Asymmetric and symmetric Si—O stretching in Q^3 tetrahedra in M-S-H	[39]
1090	Si-O bending in unreacted silica (shoulder)	[39]
1190	Si-O stretching in unreacted silica (shoulder)	[39]
1250	Si-O-Si bending in M-S-H	[21]
1400 to 1500	C-O stretching in carbonate ions (weak band)	[39]
1635	H—O—H bending	[39]
1650	Symmetrical bending of O—H bonds belonging to brucite	[42,92]
3200 to 3600	Mg-OH stretching in M-S-H phase	[92,104]
3440	Stretching of O—H groups, attributed to water adsorbed to surface/incorporated in the M-S-H structure	[5]
3550 to 3600	Stretching of O—H groups, attributed to water coordinated to Mg in sepiolite	[42,105]
3680	Mg-OH stretching in M-S-H phase	[39,42,102]
3692	Stretching of O—H groups in unreacted brucite (sharp band)	[39]
3700	Symmetrical stretching of O—H bonds belonging to brucite	[42,92,106]

^a Vibrational modes from unreacted silica are centred at higher end of the band [21].
^b Shifts to lower wavenumbers as Mg/Si ratio increases [41].

resemblance to serpentine group minerals like antigorite or lizardite [42].

Nied et al. suggested that such an increase in the Mg/Si ratio leads to silicate depolymerization [39]; a serpentine-like structure is reported to be favoured at high Mg/Si ($\geq$ 1) ratios, while lower Mg/Si ($\leq$ 1) ratios lead to a talc-like structure [4]. The presence of Q^2 in the ^{29}Si MAS NMR spectra of M-S-H was related to the nanocrystalline size of the M-S-H phases [40]. For example, the proportions of Q^3 and Q^2 species (calculated via ^{29}Si MAS NMR analyses) in an M-S-H sample with Mg/Si of 0.6 indicated characteristic dimensions of 1.5 nm (a-b plane) and 2.4 nm (c plane) for this sample, having an increase in defects in the silicate plane with increasing Mg/Si ratio [40]. SAXS measurements on M-S-H phases of Mg/Si of 1.0 were modelled with a polydisperse spherical structure with an average radius of ca. 1.7 nm for M-S-H [103].

The vibrational modes usually seen in the FTIR analysis of M-S-H phase are detailed in Table 3. The FTIR spectra of M-S-H materials usually present bands related to the stretching and bending vibrations of the O—H bonds due to absorbed water at ca. 3600 and 1650 cm^{-1}, respectively, with intensities proportional to the degree of hydration of the sample. A broad band around 1100 to 950 cm^{-1} is associated with the stretching of Q^3 Si—O groups, whereas the antisymmetric stretching vibrations of the Q^2 Si—O groups appear at ca. 950–870 cm^{-1} [3].

Fig. 11a displays the FTIR spectra of M-S-H phases with varying Mg/Si ratios (0.8 to 1.4), cured for 3 to 24 months [41]. The regions where the vibrational modes related to the different Q^n sites are shown as shaded areas, being assigned to Si sites as follows: Q^1 (780–830 cm^{-1}); Q^2 (870–920 cm^{-1}); Q^3 (950–1150 cm^{-1}); Q^4 (>950 cm^{-1}). The band seen at ca. 1016 cm^{-1} is assigned to Q$_c^3$ sites, the shoulder at 985 cm^{-1} represents Q$_a^3$ sites, and the shoulder at 957 cm^{-1} is attributed to Q$_b^3$ sites (where Q$_a^3$, Q$_b^3$ and Q$_c^3$ are sites identified by ^{29}Si MAS NMR analysis). When silica fume is used as precursor of M-S-H materials, the initial Q^4 SiO$_4$ units of silica are well seen at early ages. With time, the overall signal is a mix of the Q^4 from the silica with the Q^3 environments in the M-S-H phases. Comparing M-S-H phases with their analogous clay minerals, it is observed that the silicates are mainly organized as Q^2 and Q^3 sites, while M-S-H phases display mainly Q^3 sites.

The Raman spectra of M-S-H as a function of Mg/Si ratio are shown in Fig. 11b [39]. The samples with high Mg/Si ratio ($\geq$ 1.3) exhibit bands analogously to the Mg—O bonds of brucite at 270 and 436 cm^{-1}. Samples with low Mg/Si ($\leq$0.6) exhibit bands related to the unreacted silica between 400 and 550 cm^{-1}. The M-S-H phase has its typical polarizable modes at 175, 220, 361, 439, 668 cm^{-1}. These bands are comparable with the Raman spectrum of talc at low Mg/Si ratio, and antigorite at high Mg/Si ratio confirming the relation between the phyllosilicate structures and M-S-H phases, as demonstrated with the
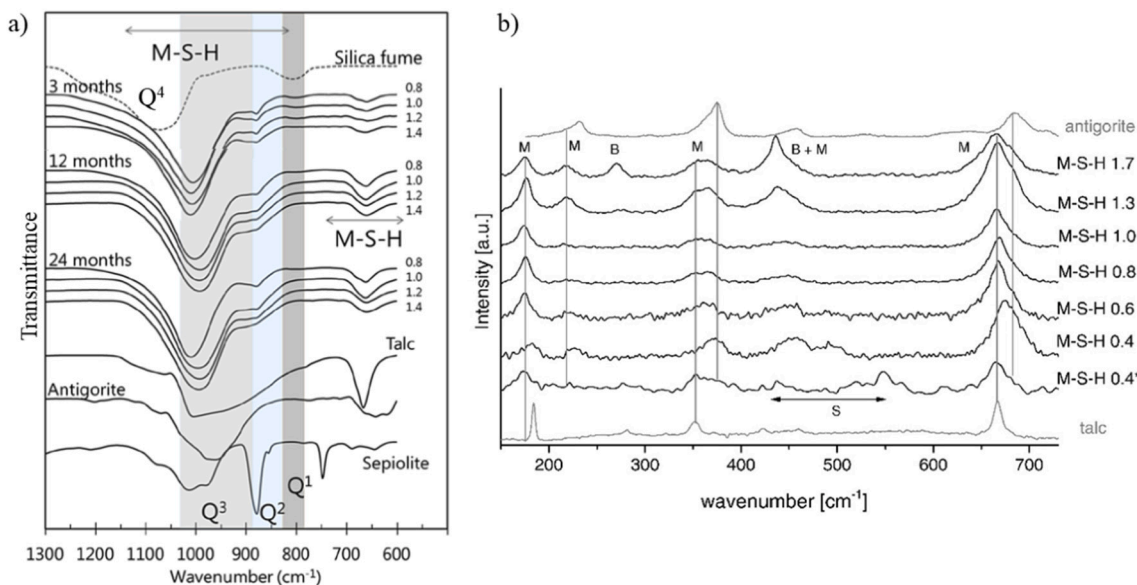
Fig. 11. a) FTIR characterization of M-S-H phases with varying Mg/Si ratio (0.8 to 1.4) cured over 3 to 24 months. The regions corresponding to various Q^n species (Q^1, Q^2, Q^3, and Q^4) are shown as shaded areas [41]. b) Raman spectroscopic analysis for M-S-H with varying Mg/Si ratio (M: M-S-H, B: brucite, S: unreacted SiO_2) [39].
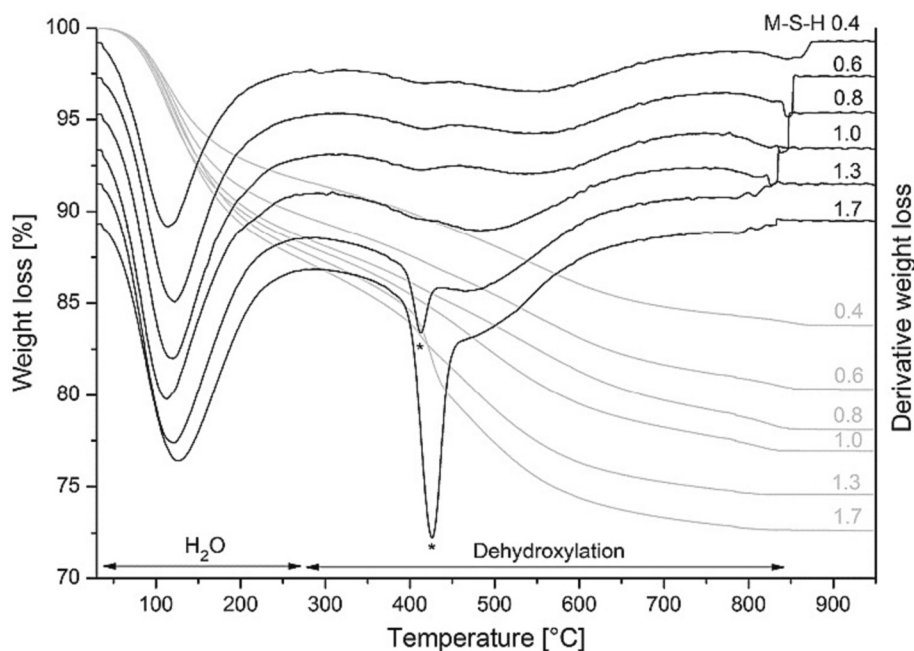

Fig. 12. Thermogravimetric analysis (TGA) for M-S-H with varying Mg/Si ratio [39].

other methods. The Raman bands of M-S-H samples are also broader (compared to talc or antigorite), which can be attributed to the nano-crystalline nature of the M-S-H phases and changes in the polarizability of the Mg—Si bonds, respectively [39].

3.3. Content of water, surface charge and microstructure of M-S-H

Fig. 12 displays the results of thermogravimetric analysis (TGA) of M-S-H phases with varying Mg/Si ratio [39], showing the initial events at ca. 30 °C and 280 °C assigned as the losses of absorbed and physically bound water from the surface, respectively [42,54]. The intensities of the signals due to these kinds of water depend on the drying conditions as well as RH; harsh drying (i.e. freeze drying) or low RH will results in a low amount of absorbed physically bound water [42]. Indeed, the water content, calculated by TGA measurement, was slightly higher than the water according to the DVS measurement.

The water loss occurring at temperatures higher than 280 °C corresponds to the dehydroxylation of M-S-H or water present as chemisorbed monolayers on the surface of M-S-H [39,40,42,54]. The samples with high Mg/Si ratios (≥ 1.3) exhibit a sharp weight loss around 410 °C related to the dehydroxylation of brucite. Bernard et al. observed that water loss at 390 °C is mainly due to the dehydroxylation of Si-OH groups in M-S-H, while the loss at 500 °C corresponds mainly to the dehydroxylation of Mg-OH groups in M-S-H [42]. The gradual and nearly continuous water loss exhibited by M-S-H is due to its non-crystalline nature [42]. The bound water and hydroxyl group content

of M-S-H increases with an increase in Mg/Si ratio [39,40]. The distinct exothermic transition revealed by M-S-H samples around 840–860 °C corresponds to the decomposition of M-S-H, leading to the formation of SiO_2 and enstatite and/or forsterite depending on the Mg/Si ratio [20,107].The ^{1}H MAS NMR spectra of M-S-H samples with Mg/Si = 0.4 to 1.7 (Fig. 10b) showed a band at 4.8 to 5.1 ppm attributed to water, along with a band at 0 to 1 ppm assigned as two components of OH groups, potentially from two different Mg-OH sites. The calculated H_2O/OH ratio decreased with an increase in Mg/Si ratio [39]. In addition, [1]H—^{29}Si CP MAS NMR investigations indicated that significant polarization is transferred from hydrogen nuclei to silicon nuclei [39], which may imply closer proximity of protons to silicate species. Hydroxyl groups bonded directly to silicon will have shorter contact times than water adsorbed on the particle surfaces. When the ^{1}H - ^{29}Si CP MAS NMR spectra were recorded for a series of contact times ranging from 0.2 ms to 5 ms, it was observed that the bands related to the Q^1 and Q^2 sites have the highest intensities between 2 and 4 ms. This suggests the presence of protons in the 2nd or 3rd coordination shell, meaning that Q^1 and Q^2 sites are present at the surface as Si-OH. The Q^3 sites appear after longer contact times (> 5 ms) [39].

M-S-H phases were studied with ^{1}H NMR relaxometry analyses [42]. The Carr−Purcell−Meiboom−Gill (CPMG) and the quadrature echo (QE) pulse sequences were employed for estimating the mobile and solid water populations. The CPMG T_2 results obtained for an M-S-H sample with Mg/Si ratio of 0.9 identified three types of chemical environment around the water molecules in the M-S-H sample: 1) *Very confined* water in the interlayer and surface; 2) *confined* water present in micro-pores; 3) *bulk* water trapped in the space between the M-S-H agglomerates. Water populations with shorter T_2 times are attributed to stronger interactions with solids (structural/solid/chemically combined water - hydroxyl groups), estimated by the QE pulse sequence. Note that QE (also TGA) cannot make the same kind of differentiation among the water populations made by CPMG analysis. Fig. 13 shows the results for the

distribution of water populations in M-S-H samples with Mg/Si ratios 0.9 and 1.2. The content of bulk water is low (<3 %), which is in the range of the background noise. The amount of confined water (present in very fine pores) is 65 % for M-S-H 0.9, while it is 56 % for M-S-H 1.2. The amount of very confined water, including the internal water present in the interlayer, the external water strongly adsorbed on the particle surface, and the coordinated water bound to Mg, is roughly 10 % for both samples [42].

Fig. 14a shows results of cation exchange capacity (CEC) for M-S-H phases. CEC estimates the amount of exchangeable cations present in the interlayer space of the silicate sheets. It was shown that M-S-H has a low CEC (30–40 meq/100 g) at pHs between 8 and 10.5, which is relatively low when compared with smectite clays (80–200 meq/100 g) [42]. However, high pHs increase the CEC of the M-S-H, reaching values of 150 meq/100 g at a pH of ca. 12.5. This implies the existence of exchangeable cations in the structure of M-S-H and relates the CEC properties with the deprotonation of the hydroxyl ions in the M-S-H structure. A study by zeta potential measurement of an M-S-H suspension showed that it was reversible [108]. That may mean a negatively charged surface in the M-S-H phases, as commonly observed in T:O:T type clays, dependent on the OH groups' protonation.

Conversely, the charges of clay minerals are due to the replacement of Si^{4+} by Al^{3+}, or Mg^{2+} by Al^{3+} and structural vacancies [109,110]. The CEC estimated for M-S-H materials is seen to increase at high Mg/Si and pH values, while the zeta potential (Fig. 14b) is also noticed to increase with pH raise (from −19 mV at pH 8.6 to −28 mV at pH 10.2). The decrease in zeta potential with increasing pH can be attributed to the deprotonation of hydroxyl groups at alkaline pH.

Quantitative electron probe microanalysis of M-S-H materials [40] showed that the water and hydroxyl content estimated for M-S-H 0.6 and M-S-H 1.2 (21.6 % and 28.1 %, respectively) were close to those calculated using TGA (19 % and 23 % respectively). The result of the dynamic vapor sorption (DVS) measurements of a M-S-H phase (Mg/Si
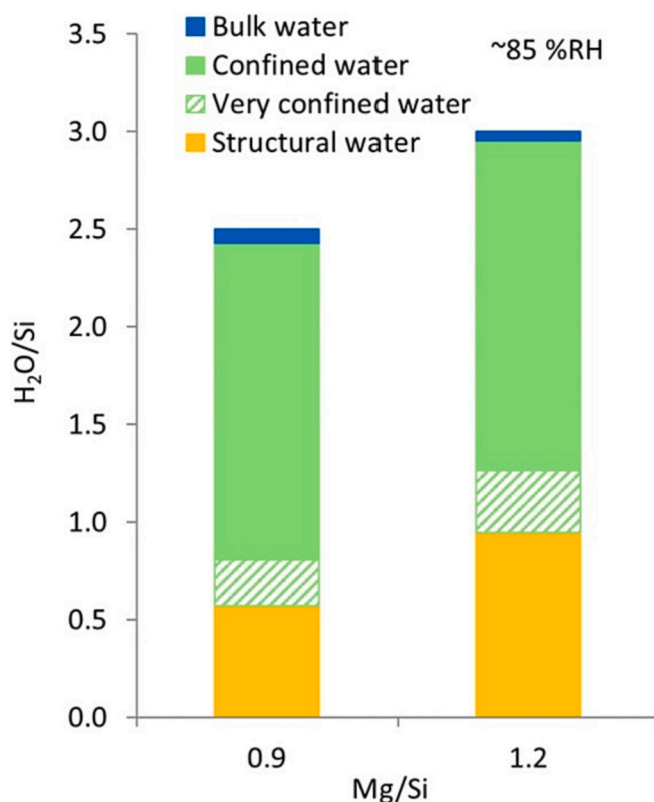

Fig. 13. Distribution of water populations in M-S-H as a function of Mg/Si. Normalization has been performed w.r.t total bound water from TGA analysis; structural water content is obtained from QE, while mobile water content is obtained from CPMG [42].
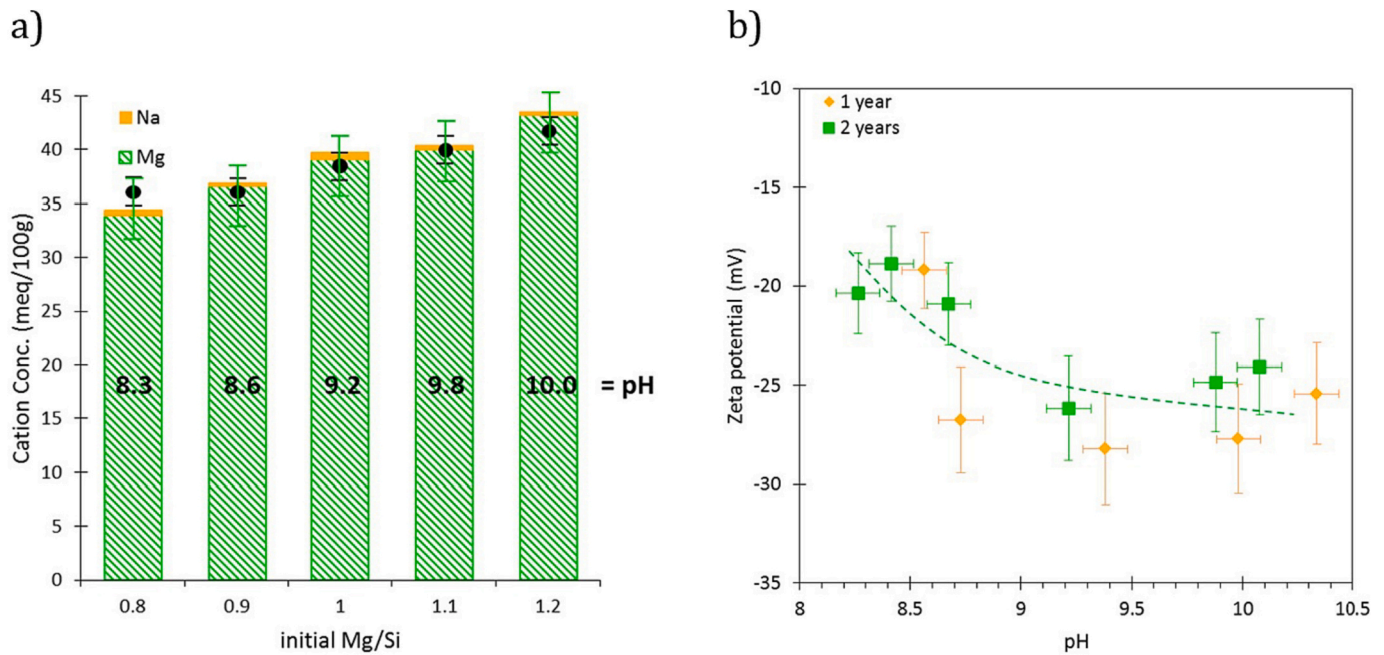
Fig. 14. a) The cation exchange capacity (CEC) estimated by colorimetry (black circles) and amount of cations sorbed on M-S-H (calculated by cobalt hexamine method) as a function of Mg/Si, pH of the solution at equilibrium are displayed, b) the zeta potential of M-S-H as a function of pH [42].
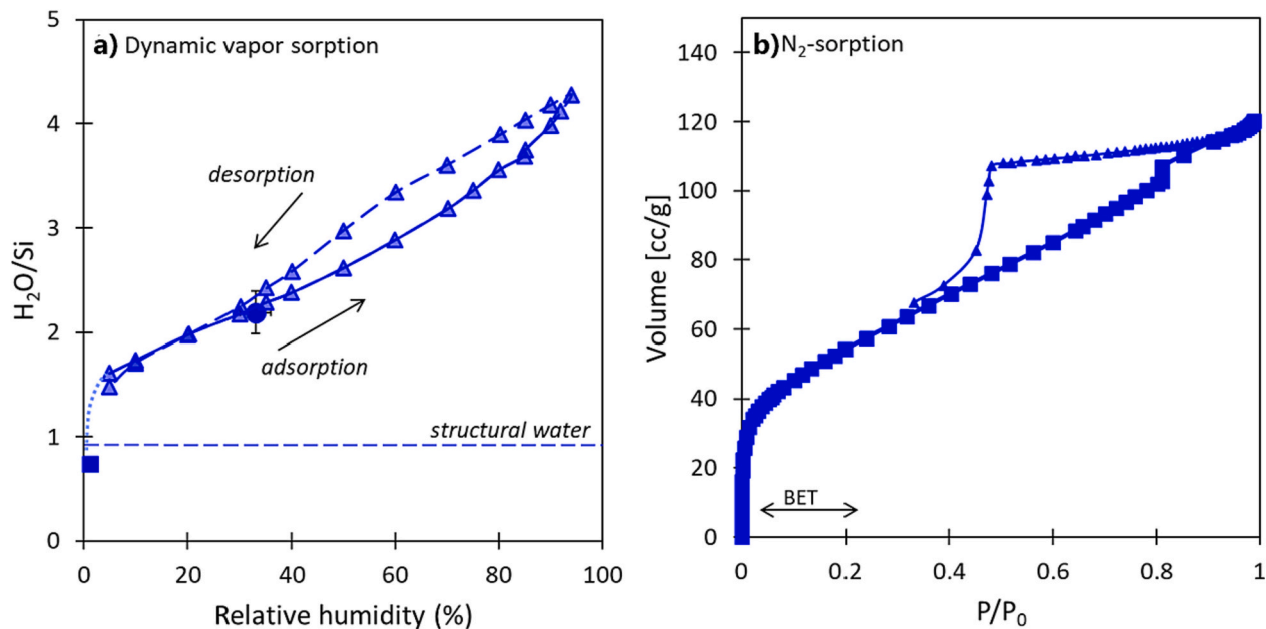

Fig. 15. a) Water adsorption-desorption isotherms for M-S-H (Mg/Si = 1.2) obtained through DVS. The square point gives the value of structural water content calculated by DVS. Horizontal dashed lines indicate the structural and total water content calculated by DVS. b) N_2 adsorption-desorption isotherms for M-S-H at Mg/Si = 1.2. Adapted from [42].

= 1.2) is shown in Fig. 15a [42]. This water sorption-desorption curve also exhibits a hysteresis loop, which is characteristic of clay minerals [111]. This behaviour is attributed to the fact that RH can control the interlayer distances (by water adsorption in the interlayer space) and also to the swelling behaviour characteristic of clays [111]. The mass shown at the end of the experiment corresponds to the dry mass of M-S-H (with no hydroxyl groups or adsorbed water on the surface but with structural hydroxyl groups).

The results of the N_2 adsorption-desorption isotherms for an M-S-H sample at Mg/Si = 1.2 (Fig. 15b) indicated a type IV shape hysteresis loop according to the IUPAC classification [112]. The initial vertical

slope is attributed to micropores (0.4 nm $\leq$ d $\leq$ 2 nm), suggesting a monolayer-multilayer adsorption processes. The hysteresis loop is attributed to the capillary condensation occurring in the mesopores (2 nm $\leq$ d $\leq$ 50 nm). The general characteristic of the isotherms is similar to those observed in synthetic phyllosilicates. The microporosity may be attributed to the interlayer space, while the mesoporosity relates to particles, as observed for T:O:T clay minerals [113]. The specific surface area of M-S-H materials is similar to values usually reported for T:O type clays but varies greatly within M-S-H materials, being observed the following trends: 1) Specific surface areas decrease with increasing Mg/Si ratio of M-S-H; 2) Specific surface area is unaffected by curing
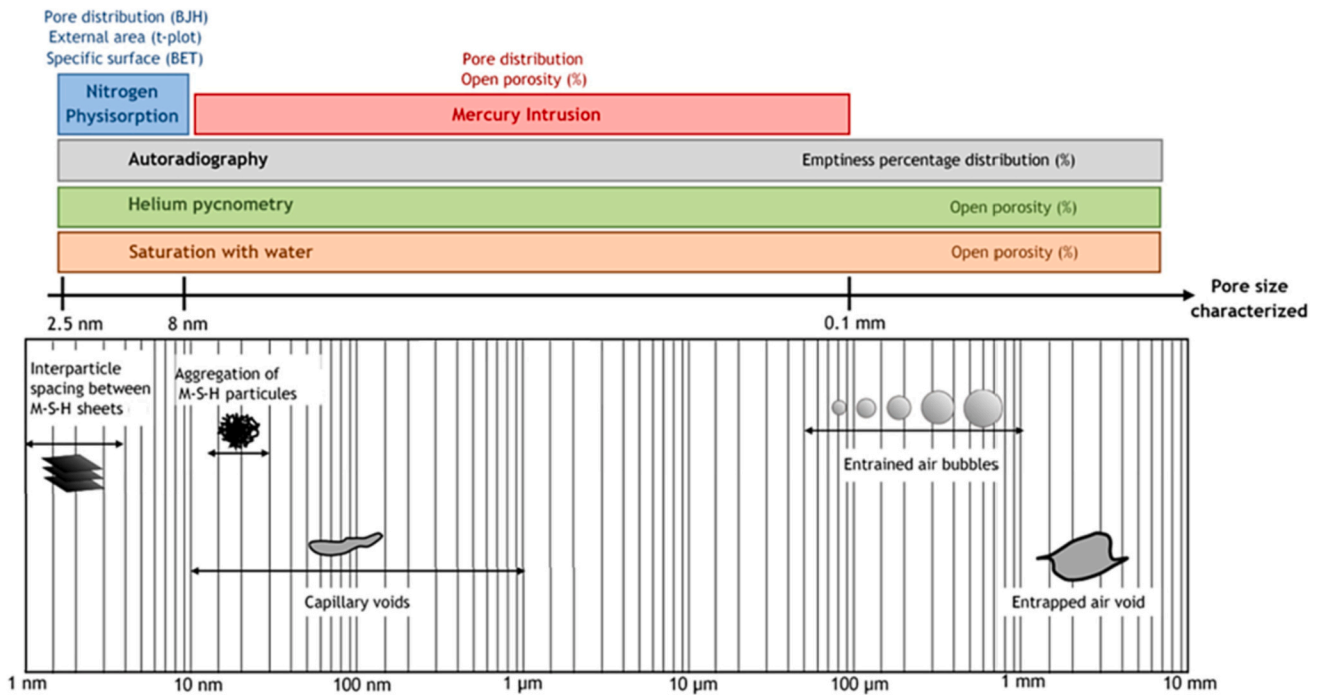
Fig. 16. The porosity estimation methods as a function of pore range associated with the microstructure of M-S-H pastes, adapted from [56].
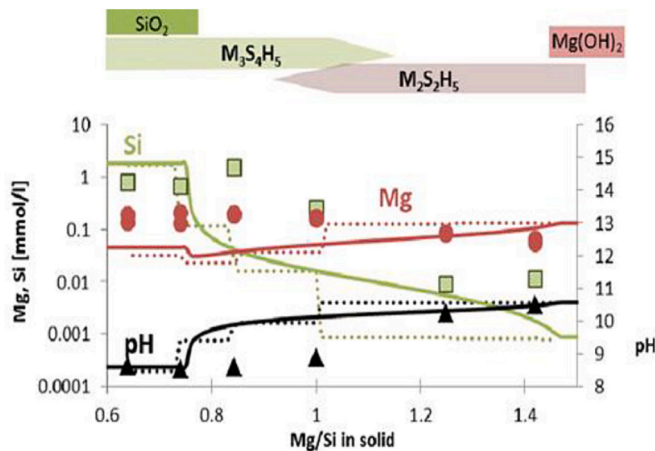

Fig. 17. Results of the solubility studies on M-S-H. Mg/Si ratio in M-S-H (triangles), Si concentration (squares) and Mg concentration (circles) as a function of Mg/Si ratio in the solid phase. Dashed lines correspond to the solubility of brucite and amorphous silica. The calculations employed used as solid solution (solid lines) between $M_3S_4H_5$ and $M_3S_2H_5$ as well as single solids (dotted lines) [39].

Fig. 18. Evolution of the solubility product at 25 °C as a function of the Mg/Si ratio (from $M_{0.75}S_1H_x$ to $M_{1.5}S_1H_y$); adapted from [41], with data from [39,117–120].

temperature; 3) Specific surface area decreases with curing time, implying the formation of larger particles [42]. Dewitte et al. confirmed that M-S-H pastes are highly porous with plate-like micro and mesopores and that the Mg/Si increase led to a reduction in specific surface area as well as micro and mesopore volumes [56].

Fig. 16 shows the porosity estimation methods as a function of pore range associated with the microstructure of M-S-H pastes [56]. In the range of capillary pores to clusters of globules, MIP analysis from Dewitte et al. indicated that mechanically mixed pastes have a mesopore distribution around 10 nm, while manually mixed pastes exhibited a mesopore distribution around 30 nm due to lower homogenization of the precursors [56]. On a larger scale, information regarding open porosity can be obtained. According to autoradiography measurements,
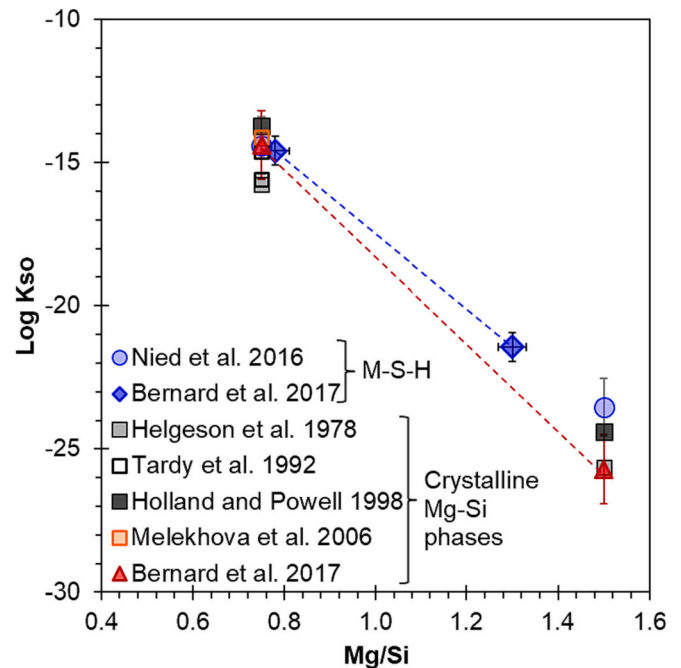
cracking of samples was observed as soon as water was removed from them. This revealed the mechanical properties and the sensitivity of M-S-H to environmental humidity. Water saturation studies can over-estimate porosity as drying at high temperatures leads to calcination of hydrates [56].

Additionally, Zhang et al. also investigated the pore structure of M-S-H mortars containing different w/b (0.5, 0.55, 0.6) and different sand contents (25, 50, and 75 %) via MIP [114]. They observed that M-S-H
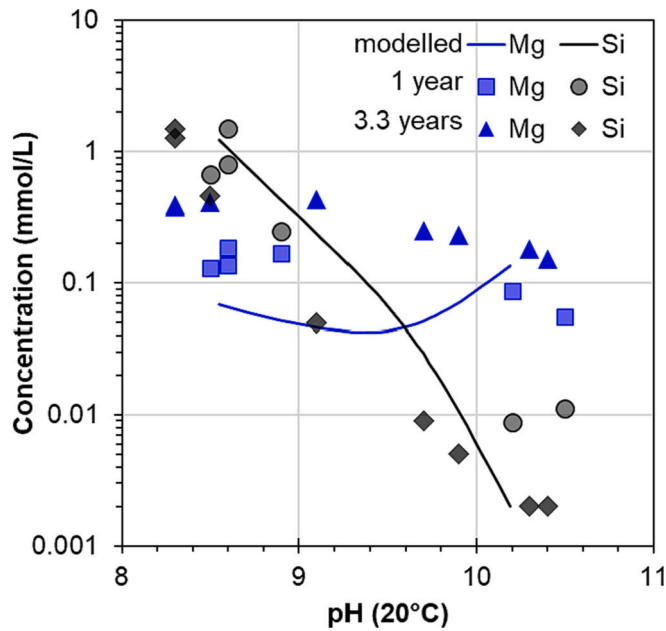
Fig. 19. Magnesium (blue symbols, squares and triangles) and silicon (black symbols, circles and diamonds) concentrations as a function of pH at 20 °C after 1 year [39] (squares and circles) and after 3.3 years [42] (diamonds and triangles), compared to the calculated solubility of M-S-H. (For interpretation of the references to colour in this figure legend, the reader is referred to the web version of this article.)

mortars possessed gel pores with size smaller than 10 nm, while PC mortars exhibited capillary pores whose size was <100 nm. This led to M-S-H mortars showing lower permeability than PC mortars.

3.4. Thermodynamic database and thermodynamic modelling

3.4.1. Thermodynamic databases

Solubility products are usually obtained from measured aqueous concentrations when the equilibrium between solid and aqueous phases is supposed to be reached. Roosz et al. calculated solubility products assuming the formation of two single M-S-H phases with Mg/Si = 0.6 and 1.2 [40]. Nied et al. calculated the solubility products for M-S-H phases based on aqueous solution composition after 1 year of equilibrium. They proposed a solid solution model based on a M-S-H with Mg/Si = 0.75 (composition of "hydrated" talc, $M_3S_4H_5$) and an M-S-H with Mg/Si = 1.5 (composition of "hydrated" serpentine, $M_3S_2H_5$) as shown in Fig. 17 [39]. The solid solution seems more adequate to the M-S-H modelling due to the nano-crystalline character and variable composition (large range of Mg/Si) as modelled for C-S-H with similar features [115]. While the approach of Nied et al. was to reach the equilibrium from oversaturation after 1 year [39], the solubility products of M-S-H can be determined via different temperature, time, and undersaturation conditions [41]. A comparison between the different solubility products found in literature for M-S-H and the crystalline phases is presented in Fig. 18. The solid solution approach, represented by the solid lines shown in Fig. 18, is compared to the separate solubility product estimated for each experimental composition (dotted lines in Fig. 18, or approach used in [116]). However, descriptions of single phases might nonetheless be useful to reduce the computational time required for reactive transport modelling, which can be time-consuming when using solid solutions.

Fig. 19 shows calculated dissolved Mg and Si concentrations as a function of the pH based on these solubility products and compared to experimental data collected from the literature. Surprisingly, the dissolved Mg is higher after 3.3 years than after 1 year, where the solution is supposed to be closer to equilibrium and, therefore, lower in dissolved

Table 4
Thermodynamic properties of M-S-H found in literature, for standard conditions (25 °C and 1 atm).

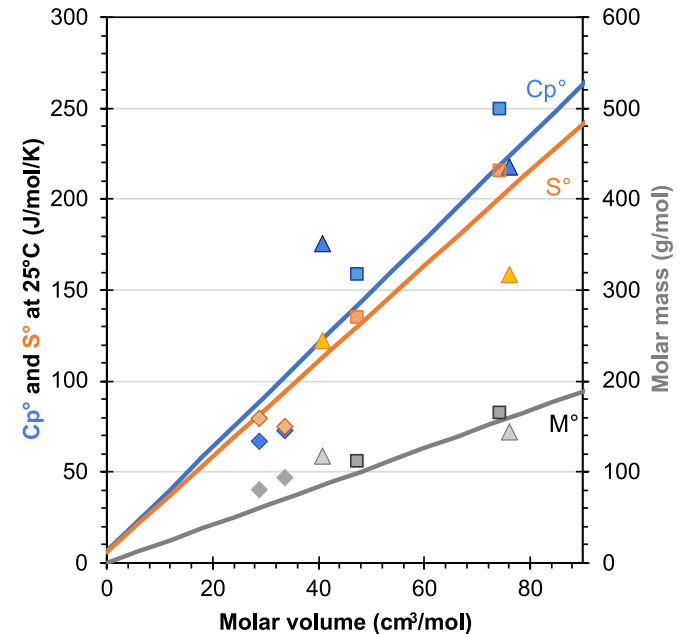| Phase	Molar mass (g/mol)	Heat capacity at 25 °C (J/mol/K)	Entropy at 25 °C ((J/mol/K)	Molar volume (cm³/mol)	Ref
$M_{3/4}SH_{5/4}$	112.9	159	135	47.4	[35,123]
$M_{3/2}SH_{5/2}$	165.6	250	216	74.3	[35,123]
$M_{0.8}SH_{1.5}$	118.2	176	123	40.9	[130]
$M_{1.3}SH_{1.8}$	144.9	218	159	76.1	[130]
$M_{0.6}SH$	81.1	67	80	28.8	[116]
$M_{1.0}SH$	95.1	73	75	33.7	[116]

Fig. 20. The correlation (lines) of heat capacity, entropy, molar volume, and molar mass of M-S-H with the data obtained from [39] (square), [130] (triangle), [116](diamond).

species concentration [41]. This could be due to a slight carbonation of the solution over time, and a resulting complexation between the dissolved carbonates and magnesium, increasing the Mg concentration as detailed in [80].

Based on the solid solution model for M-S-H, this phase can incorporate different ions into its structure. The partial incorporation of Ca in M-S-H could happen with an estimated maximum degree of Ca/Si ~ 0.1 (in suspension experiments). Solubility products for M-C-S-H were calculated from aqueous solutions in [121] in conjunction with the solid solution model from [41]. Single phases were also derived for reactive transport modelling [122]. Aluminium was also observed in the M-S-H, leading to the description of M-A-S-H [82], but only a few solution analysis data measured at equilibrium with such phases could be found in literature. Bernard et al. calculated the ion activity products for $M_{0.75}A_{0.2}S_1H_{1.5}$ and $M_{1.5}A_{0.2}S_1H_{1.8}$ based on aqueous analysis and compared them to clay minerals with similar compositions, such as vermiculite or saponite [82]. The M-A-S-H phases seem to present similar stability to these clay minerals. Recent thermodynamic modelling predicted the formation of M-A-S-H in the MgO-Al₂O₃-SiO₂ system, considering the formation of an ideal M-A-S-H solid solution based on M-S-H, using data provided in Cemdata 18 [123] and M-A-S-H ion activity products provided in [82]. In a similar system but under highly alkaline conditions (NaAlO₂-Mg(OH)₂-SiO₂-H₂O), M-A-S-H were not observed,
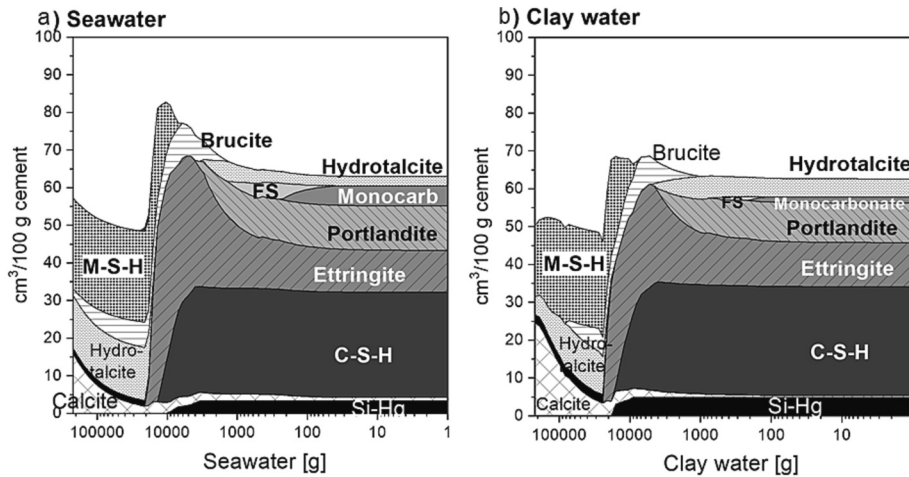
Fig. 21. Predicted volumes of the phases in the PC paste upon exposure to increasing amounts of a) seawater (from [131]; and b) of clay water (adapted from [132]) In each case, the left side of the plot represents the exposed surface, and moving to the right (lower addition of the leachant) indicates moving into the bulk of the sample, with the unexposed material at the right-hand side of the plot.

but zeolite and hydrotalcite formed instead [124].

Another interesting ion to incorporate in M-S-H is Fe, which was observed in M-S-H in geological environments during the precipitation of this phase due to the serpentinization of olivine-rich rocks (Mg, Fe)$_2$SiO$_4$ [83]. The natural weathering decreases Mg/Si in the main solid from 2 to 1.5 (serpentine: (Mg,Fe)$_3$Si$_2$O$_5$(OH)$_4$) and leads to brucite formation. The brucite induces high pH values (~10.5), with the partial dissolution of quartz, and results in dissolved Mg, Fe, and Si, ready to react into M-S-H [125]; recent work observed Fe in the M-S-H formed [119]. However, no exact Fe/Si is reported, and thermodynamic data are not yet available. Similarly, no incorporation of alkalis in the M-S-H

has been thermodynamically described yet.

3.4.2. Molar volume, heat capacity and entropy

Bernard et al. [41] estimated a temperature-dependent heat capacity, C°$_p$ for M-S-H from the data for talc, chrysotile, and antigorite given in [119] and adjusted for the water content of the M-S-H phases (Table 4). The entropy, S°, was calculated similarly for talc, chrysotile, antigorite, and water. These values were in the same range of the heat capacity and entropy of the hydrated phases deduced by Roozs et al. [116] from the measured heat capacity of the anhydrous phases and the water content of the M-S-H phases, considering the heat capacity of

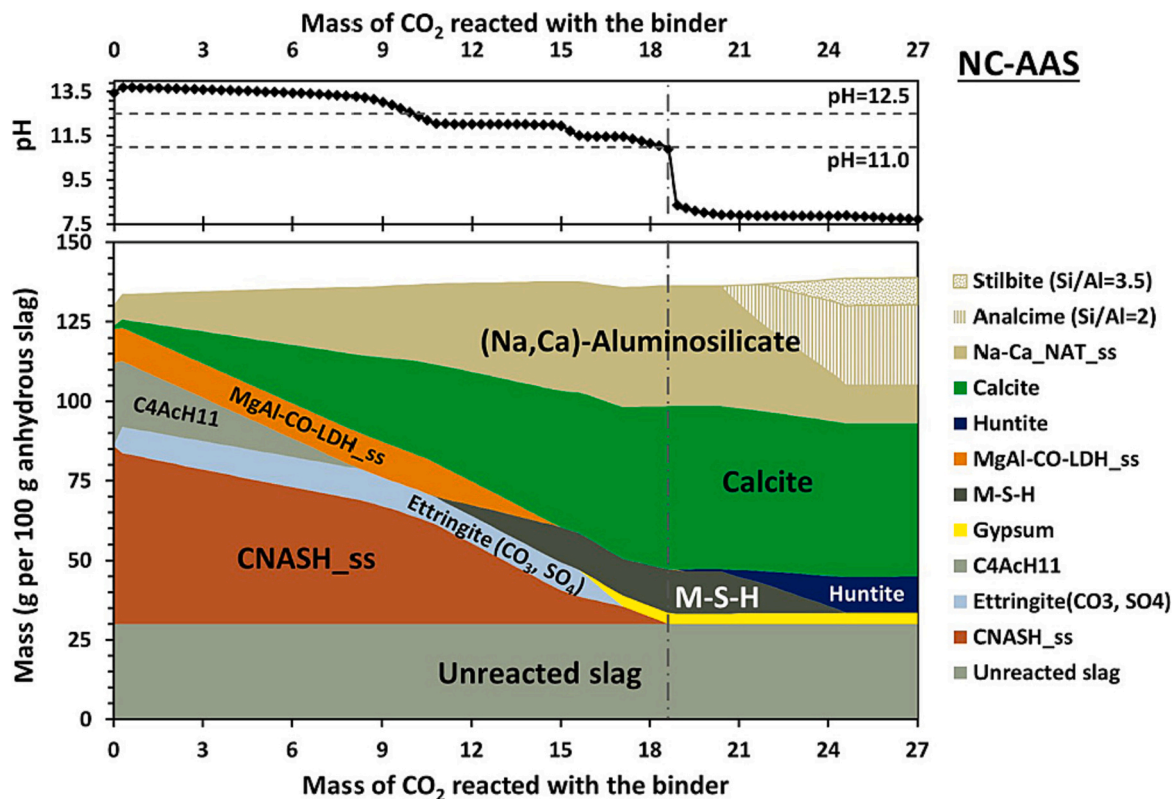**Fig. 22.** Phase assemblage of Na$_2$CO$_3$-activated slag paste (4 % Na$_2$O, degree of slag reaction 70 %) predicted under step-wise accelerated carbonation (1 % CO$_2$), and the corresponding pH in the aqueous phase (pore solution), reproduced from [133].
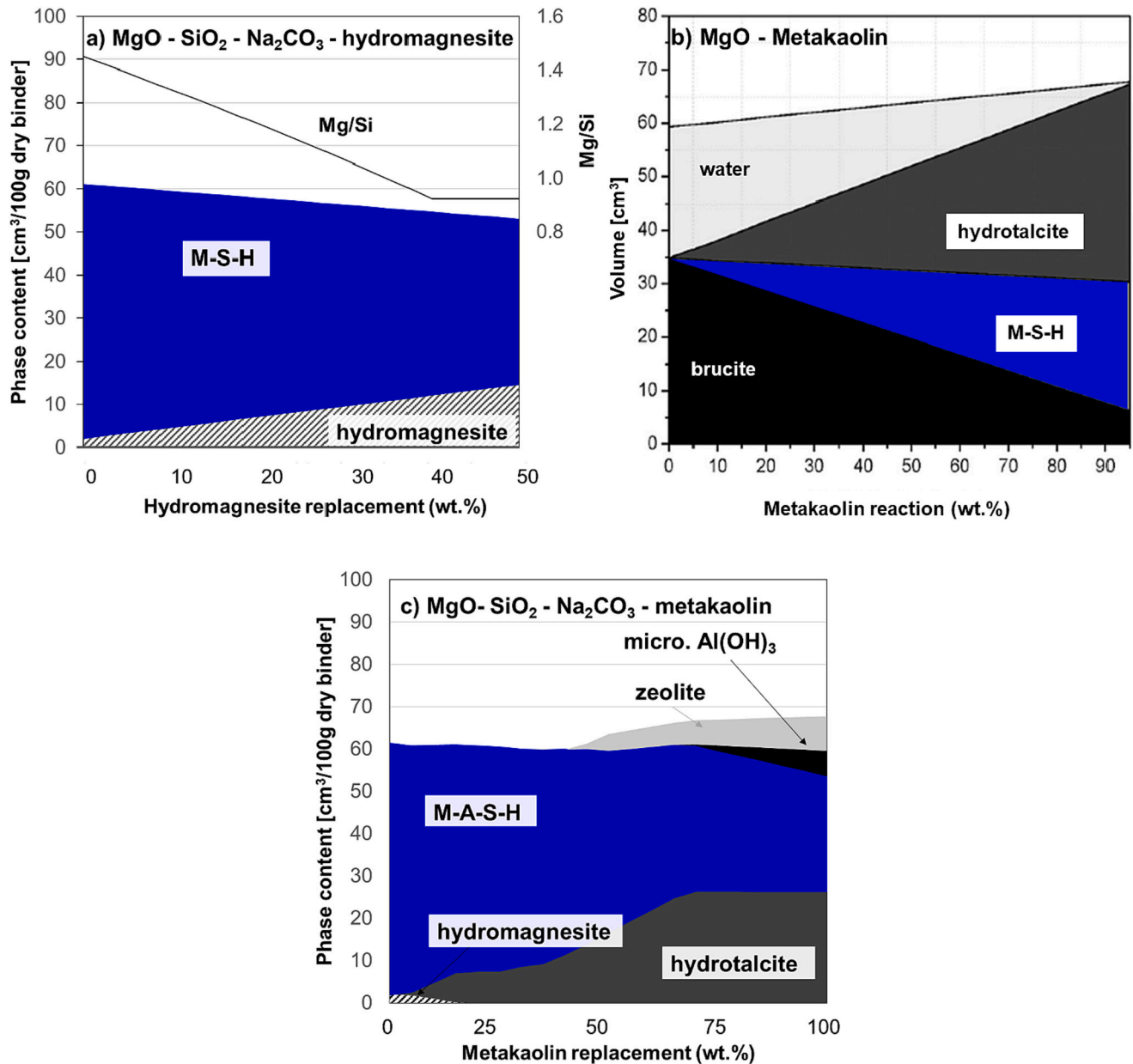
Fig. 23. Thermodynamic modelling of Mg/Si = 1.5 systems: a) from [80], with adapted thermodynamic data for hydromagnesite as detailed in [80] b) adapted from [64], depends on the reaction metakaolin, thermodynamic data from cemdata18 [123]; c) calculated for this review based on the recipe from [138] and full reaction of the metakaolin; adapted thermodynamic data for M-A-S-H (ideal solid solution between M-S-H with data provided in Cemdata18 [123] and M-A-S-H ion activity products provided in [82] and carbonated hydrotalcite from [137].

hydration to be negligible. Fig. 20 displays the $C°_p$, the $S°$, and the $V°$ given in literature, depending on the molar mass of the M-S-H. We also assessed the correlations between the three properties in order to provide an approach to estimate the $C°_p$, $S°$ and $V°$ when molar mass of M-S-H or its one of these thermodynamic properties is known. The standard entropy can be estimated from the formula unit volume [V_m, i.e., derived from $V° \times 10^{21}/(6.02 \times 10^{23})$] as proposed by Jenkins and Glasser [126] using the following formula: $S° = 1579 \times V_m + 6$ for ionic hydrates. In addition, the heat capacity $C°_p$ shows a strong linear correlation with standard entropy $S°$ as expressed by $C°_p = 1.089(\pm 0.012) \times S°$ through the Debye equation [127]. The empirical Neumann–Kopp (NK) rule [128,129] can also be used to estimate the heat capacity of M-S-H based on the sum of the heat capacity of each oxide in the phase. Lastly, the molar volume $V°$ correlates with molar mass via $V° = M°/\rho$ where ρ (2–2.1 g/cm^3) is the density of M-S-H as reported in [42].

3.4.3. Thermodynamic modelling

Since M-S-H thermodynamic data are included in standard thermodynamic databases, most of the thermodynamic modelling of degradation of Portland-based cement in Mg-rich environments such as seawater or clay water usually predicts M-S-H formation, for example, as shown in Fig. 21. The calculations mimic the degradation of concrete near a solution by increasing the amount of exposure solution. Leaching of Ca-rich phases is the main degradation mechanism predicted, as visible in the destabilisation near the surface of portlandite, of AFm phases such as mono-carbonate and Friedel's salt, and of C-S-H. The changes at the cement surfaces in contact with Mg-rich solution lead to the precipitation of M-S-H and hydrotalcite, together with ettringite and calcite. With more extensive leaching, all Ca-containing hydrate including ettringite becomes destabilized, leaving only M-S-H with hydrotalcite and calcite. In slag-based alkali-activated materials [7], hydrotalcite is the main Mg-

containing phase, as the slag often contains up to 10–12 wt% MgO in its chemical composition. Under carbonation, the alkali-activated slag was predicted to form M-S-H after the degradation of hydrotalcite-like phases (Fig. 22).

Finally, including the M-S-H thermodynamic data in the thermodynamic database allowed the calculation of M-S-H formation as the primary product in MgO-based cements. Fig. 23 shows different models of MgO-silicate sources for cements with Mg/Si = 1.5. The first model (Fig. 23a) corresponds to the formation of M-S-H in a carbonated environment (Na_2CO_3 and hydromagnesite) [80]. Under these conditions, the modelling shows the formation of M-S-H and the stability of hydromagnesite. The precipitation of hydromagnesite is preferred when the concentration of carbonates is sufficient. However, in the experiments where MgO and SiO_2 are blended with hydromagnesite, mainly M-S-H is formed and hydromagnesite partially reacts, which contradicts the thermodynamic modelling. In a MgO-CO_2-H_2O chemical system without silicate, Winnefeld et al. [134] modelled artinite precipitation but did not experimentally observe the phase, or some new carbonate species (e.g., amorphous magnesium carbonate [135] and giorgiosite-like crystal [136]) were reported without known thermodynamic data. Therefore, achieving better consistency and accuracy in thermodynamic data as well as determining thermodynamic data of new carbonate species are needed to improve the thermodynamic modelling of different blends in the MgO-SiO_2-CO_2-H_2O system.

Recent modelling based on the Cemdata18 database modelled the reaction effect of metakaolin on the MgO-metakaolin reaction products (Fig. 23b). The hydration of MgO alone results in brucite. However, when the degree of reaction of metakaolin is higher, more brucite reacts with metakaolin, forming M-S-H and hydrotalcite. Notably, the thermodynamic data of hydrotalcite as presented in the Cemdata18 database indicate the high stability of this phase, which appears to mismatch with the actual stability of hydrotalcite, as discussed in [137]. Additionally, the M-S-H included in that database does not include the incorporation of Al in the structure. Therefore, the thermodynamic modelling of the complete reaction of the metakaolin results in more hydrotalcite than M-S-H, which is inconsistent and contrastive with experimental observations. Fig. 22c shows the modelling of the replacement of silica fume by metakaolin, using an updated database as follows: 1) carbonated hydrotalcite [137]; 2) M-A-S-H ideal solid solution (between M-S-H with data provided in Cemdata18 [123] and M-A-S-H ion activity products provided in [82]. The blend of MgO-micro silica indicates only the formation of M-S-H. When increasing the presence of metakaolin in mixes, hydrotalcite forms while the fraction of M-A-S-H reduces. With

this updated database, the modelling predicted a slightly different phase assemblage in the hydrated sample than that of the MgO-metakaolin mix (Fig. 23b). The modelling shows a larger or similar amount of M-A-S-H compared to hydrotalcite, while the presence of micro crystalline Al$(OH)_3$ and the precipitation of zeolite phases are also predicted. No crystalline zeolite or Al$(OH)_3$ could be experimentally observed, but the presence of traces of N-A-S-H or amorphous Al$(OH)_3$ could not be excluded.

4. Mechanical and durability properties of M-S-H

Mechanical and durability properties are among the most crucial engineering properties of materials needing thorough investigation prior to their use in building and construction applications. This becomes critical for alternative cements, such as M-S-H binders, being dependent on the targeted applications. Like PC-based concrete, the mechanical properties of M-S-H binders are also influenced by various factors such as w/b ratio, nature of material used in the synthesis of M-S-H binders, aggregate type, and content, addition of fibers, and curing conditions.

4.1. Mechanical properties

Overall, M-S-H binders are reported as phases of high compressive strength, which is noticed to increase with reduction in w/b. Regardless of the w/b ratio, the compressive strength of M-S-H materials increases with time, indicating progressive hydration of the M-S-H binder over time. For instance, the M-S-H pastes (Mg/Si = 0.4 to 0.8) with 1 % SHMP at different w/b ratios (Fig. 24) reached over 70 MPa in compressive strength [1]. The highest compressive strength of around 70 MPa was observed for the M-S-H pastes prepared with a w/b ratio of 0.4 (after 28 days) while the w/b ratio of 0.8 reduced the compressive strength to ca. 25 MPa over the same hydration time. The compressive strength of obtained M-S-H concrete (MgO-SiO_2 concrete from a mixture of MgO, micro silica, coarse aggregates and 2 % SHMP) reached 65 MPa after 28 days [139]. M-S-H materials can display a wide range of compressive strength depending on its mix recipe, reaching similar compressive strength to higher grades of PC specified in standardized procedures (often set as 52.5 MPa characteristic strength for a standard mortar after 28 days).

Based on the studies detailed previously (gathered in Table 1 in Appendix), the compressive strengths (after 28 days) of M-S-H binders as a function of the w/b ratio and type of superplasticizer are compiled in
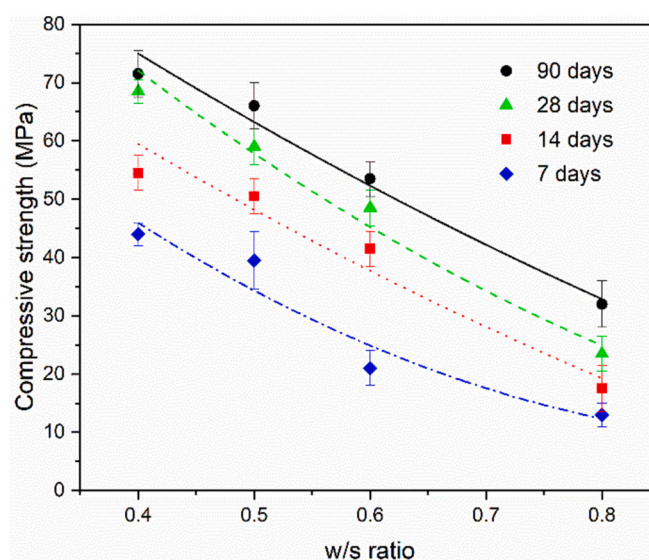

Fig. 24. Compressive strength of M-S-H binder (Mg/Si = 0.97) synthesized with 1 % SHMP at different w/b (reproduced from Ref. [1]).
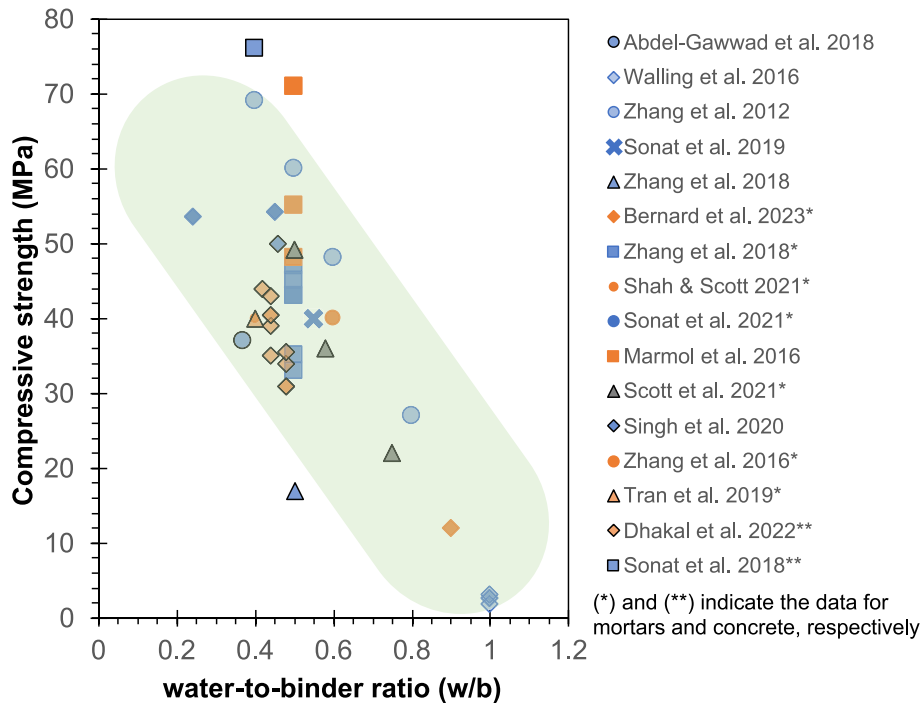
Fig. 25. Compressive strength (after 28 days) of M-S-H binders as a function of the w/b ratio and type of admixtures used in which blue = SHMP and orange = PCEs while gray = no additive (plot based on studies provided in Table 1). (For interpretation of the references to colour in this figure legend, the reader is referred to the web version of this article.) (For interpretation of the references to colour in this figure legend, the reader is referred to the web version of this article.)
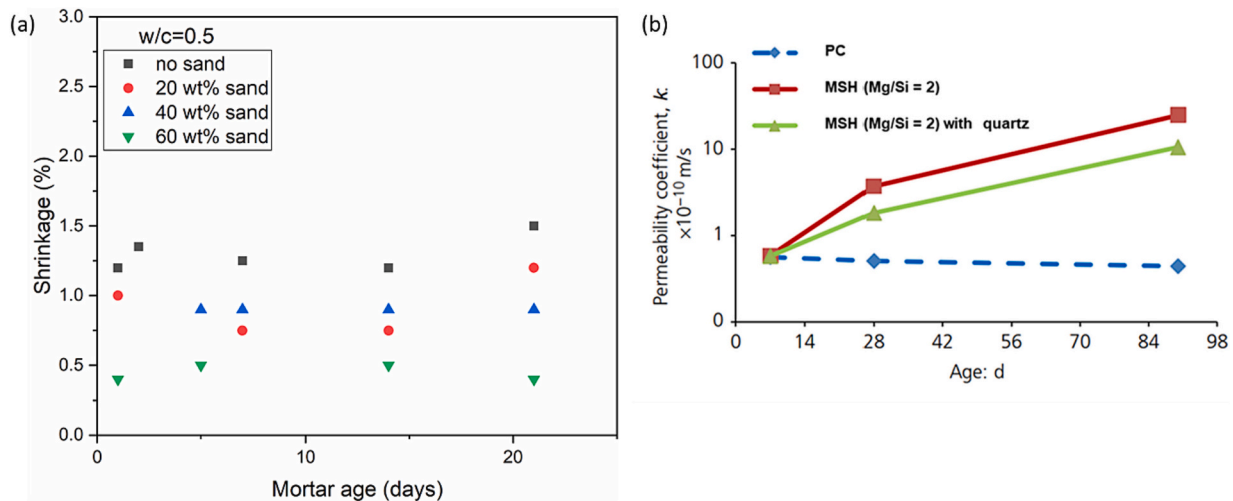

Fig. 26. a) The drying shrinkage of M-S-H binder (Mg/Si = 1) prepared with w/b = 0.5 and different sand addition (reproduced from Ref. [141]) and b) Oxygen permeability coefficients of M-S-H binder and hydrated PC [145].

Fig. 25. The compressive strength of M-S-H materials might follow the Gel-Space Ratio concept, which relates the influence of porosity on the strength. However, it seems that the binder containing the highest M-S-H phases does not present the highest compressive strength [140]. The compressive strengths of the M-S-H binder are related to the M-S-H gel content, but most likely to the void content created by unreacted water, indicating that the gel-space ratio is an important parameter influencing the compressive strength.

The type of precursors used to synthesize M-S-H binders also influences the mechanical properties. Apart from SF and MS, silica can also be sourced from other precursors such as metakaolin, fly ash, rice husk ash (RHA), waste glass, slags, clay, etc. [21,52,57–60]. The M-S-H produced from metakaolin has a denser and finer microstructure when

compared to the M-S-H produced using SF [57]. Metakaolin also led to the formation of hydrotalcite in addition to the M-S-H phase, which is postulated to be the main reason for the difference in microstructure development [64].

In contrast, fly ash as a precursor is reported to exhibit low reactivity for M-S-H formation and reduced mechanical strength [22,61]. Two forms of RHA (crystalline and amorphous) were recently compared to MS as a silica precursor for preparing M-S-H binder [58]. The sample with amorphous RHA produced highest early-age compressive strength, while the sample with crystalline RHA produced the lowest strength. In the long term, both RHA samples could not reach the same strength as the sample using MS. Furthermore, it was observed that the addition of CaO influences the pH value of the solution, and an increase in the mass

of CaO added can reduce the amount of M-S-H binders formed [63].

4.2. Durability properties

The dimensional stability of M-S-H binder has been consistent with the observations reported for PC binders [141]. For example, the w/b ratio is proportional related to the shrinkage of M-S-H (Mg/Si = 1) mortar [141]. To mitigate cracks from drying shrinkage in the mortar, the authors used sand with different additions and found the drying shrinkage decreased with sand addition. The results of the study in the case of M-S-H binder prepared with w/b = 0.5 are shown in Fig. 26a. The sample with 60 wt% sand addition exhibited the lowest shrinkage and did not produce shrinkage cracking. This can be explained using a simple geometrical particle packing model, according to which the net shrinkage in M-S-H was predicted to be reduced to zero when the volume of sand addition reaches around 0.77. Notably, the influence of MgO (i.e., from unreacted precursor) on dimensional stability in the M-S-H binder is also an essential factor and deserves more attention. As the late reaction for MgO can occur in the hardened sample, this can cause high crystallization pressure in the confined matrix [142], leading to deleterious crack formation (see examples for cracks caused by late reaction of MgO [143,144]. For this reason, the presence of unreacted MgO is considered highly detrimental in the M-S-H binder. However, similar later-age expansion effects have not explicitly been identified in M-S-H based binders, but this area merits further attention if these materials are to be used in important engineering applications.

Permeability and diffusivity in M-S-H binder can strongly influence its performance and durability in the long term. The oxygen permeability was used to estimate the gas permeability coefficient (Fig. 26b) [145]. The authors found that oxygen permeabilities of M-S-H binder are comparable with hydrated PC after 7 days of curing. However, during further hydration, the permeability coefficient of PC decreased while that of M-S-H binder increased. The decrease in permeability coefficient of hydrated PC could be attributed to the densification of its microstructure with ongoing hydration, while the increase in oxygen permeability of M-S-H could be due to the following reasons: 1) Increase in the level of pore connectivity; 2) microcracking associated with the formation of M-S-H; and 3) reaction of brucite with silica to form M-S-H leading to a reduction in the total volume of hydrated products. Dhakal et al. performed oxygen permeability experiments on M-S-H concrete specimens prepared from MgO and metakaolin [146]. The authors observed that permeability of M-S-H concrete was lower than the PC concrete. The authors attributed the improved performance of M-S-H concrete to the pore filling nature of hydrotalcite phases formed in the system. Zhang et al. investigated the chloride ion penetration resistance of M-S-H mortars with different w/b ratios (0.5, 0.55, and 0.6) and different sand additions (25, 50, and 75 mass % by mass) [114], observing that the chloride ion diffusion coefficient becomes larger as both w/b ratio and sand addition increase. However, the chloride ion diffusion coefficient of M-S-H mortars was found in that study to be much smaller than that of comparable PC mortars. Notably, since the pH of M-S-H binder is considered as a low-pH cement ranging from 7 to 10.5, the steel rebar can already become vulnerable to corrosion, and thus, chloride penetration may not be a critical risk factor. However, more efforts are needed to assess other durability aspects of this binder such as stability in different chemical environments e.g., sulfate and carbonation.

The use of additives as aggregates or fibers was reported in the literature to improve the mechanical performance and durability of M-S-H binders. Tran et al. used crushed quartz as aggregate in M-S-H mortar and observed that the addition of this type of aggregate led to the following: 1) increased mechanical properties (compressive strength, elasticity modulus, and tensile strength); and 2) reduced porosity and permeability in the mortar [145]. In addition, using fibrous reinforcement also enhanced the mechanical performance of the fiber-reinforced M-S-H composite [140]. The composite was subjected to 4-point

bending testing, and after 200 wet-dry accelerated aging cycles, the cellulose-reinforced M-S-H system exhibited no significant reduction in modulus of rupture or changes in deformation at the rupture point.

5. Potential applications

As discussed in Section 2.4, the structure and performance of M-S-H binders vary according to the composition and the synthetic parameters. The high strength development of the materials (up to 70 MPa at 28 days), low pH, and thermal properties can enable several applications in construction. However, we found that more efforts in research and development are needed to 1) better understand how the M-S-H binders comply with current construction standards (e.g., performance, durability, and suitable rebar) for both structural and non-structural applications and 2) seek potential novel applications both inside and outside the construction industry.

Although the low pH of M-S-H binder opens challenges for using this binder in steel reinforced concretes, this characteristic makes M-S-H binder promising material for various applications such as nuclear waste management. In such applications, Portland cement is avoided in the construction of radioactive waste deposits due to its high pH, which can reach 13.5 [147,148], leading to the partial dissolution of the clayey rocks [149,150] or the swelling of clays [151,152] with the formation of a disturbed zone at the interface. This can be associated with an opening of the porosity [153,154] and modify the transport properties of the repository system overall (e.g., water saturation, preferential flow paths, gas escape). Thus, low pH cements are needed for building radioactive waste disposal in a geological repository without affecting the impermeability of the repository, also avoiding the degradation of the surrounding clays.

M-S-H binders were proposed as a stabilizing cement for clay backfills in nuclear waste management due to their potential for excellent structural stability [20,44]. M-S-H binders can also be used to directly encapsulate hazardous nuclear wastes, as the low pH of M-S-H can serve as an encapsulation matrix for nuclear wastes containing metals that may corrode at higher pH [43]. The M-S-H cements could also be used for immobilizing $Mg(OH)_2$-rich Magnox sludge (i.e., a legacy waste of the UK nuclear industry) [5]. $Mg(OH)_2$ can be used directly as a precursor for M-S-H production (rather than MgO), leading to a high potential for very high waste loading through the production of M-S-H cements. Such low pH cements are also of interest for radionuclide or wastes retention [3]. In addition, the structure of M-S-H also offers the potential to use in waste management: 1) disposal of dredged contaminated sediments by conversion into construction materials with satisfactory mechanical strength and good toxic metal immobilization capability [46]; 2) stabilization of hazardous lead glass sludge through the production of lightweight building bricks [45]; 3) immobilization of a variety of cations including (Li^+, Ba^{2+}, Cs^+, Cr^{3+}, Co^{2+}, Ni^{2+}, Cu^{2+}, Zn^{2+}, Pb^{2+}) [3]; and 4) immobilization of radioisotopes of Cs and Sr [2,155].

M-S-H binders can be employed as structural and non-structural building component production due to their high strength development. The low pH of the pore solution of M-S-H binders makes them also a suitable matrix for natural fibers [140,156], promoting their use in applications involving natural fiber reinforcement such as low-density thermal insulating board such as earth-hemp blocks [157]. M-S-H binders are also printable in 3D printers with a control of the extrudability, shape retention, and buildability [47]. However, further research is needed to test the suitability of M-S-H binders used in construction and their long-term performance and durability.

The excess $Mg(OH)_2$ present in the M-S-H binders could react with CO_2 to form magnesium carbonates such as nesquehonite ($MgCO_3 \cdot 3H_2O$) [48]. The possibility of capturing CO_2 in the M-S-H binder was advanced as best to 260 kgs/ton binders while significantly enhancing the mechanical properties of the binder due to the carbonation [48]. Another case, where M-S-H phase and $Mg(OH)_2$ were both present in the M-S-H binders formed nesquehonite under carbonation

(20 % CO_2) [158]. However, it is unclear what are the carbonation extent and changes in M-S-H phase toward carbonation. In addition, the duration of carbonation can negatively affect the compressive strength of M-S-H binders due to the excessive carbonated phases formed. Furthermore, M-S-H binders synthesized from olivine were studied aiming to enable a suitable binder for Martian construction applications considering the locally abundant raw materials [159].

The M-S-H binders also attracts several other applications outside the construction industry. The high specific surface area [160] and adsorption properties of the binders can enable their uses in biodiesel purification [49], dye removal [161,162], removal of basic brown and chrysophenine [163], removal of anionic dye from aqueous solution [164], and catalytic cracking [165]. An interesting research direction is to improve the adsorption capacity of M-S-H phases by increasing the surface area and tuning the pore distribution to have nanosized/mesoporous/hierarchical/sandwich-type M-S-H materials [161]. Furthermore, the thermal decomposition of M-S-H binders makes them promising materials for producing refractory castables [50,51]. Here, the binders become a component in the green body of castables, and after thermal treatment, they produce enstatite ($MgSiO_3$) and forsterite (Mg_2SiO_4) [166] as refractory phases. The M-S-H content in magnesia-based castable is known to 1) reduce the hydration of Mg to form $Mg(OH)_2$ that can abruptly decompose and release water vapor, leading to a potential explosion during fast drying) [50,51,167]; 2) reduce cracking in castable; 3) improve the binding strength in castable [167].

Overall, numerous potential applications of M-S-H binders were explored owing to their unique properties. However, further studies regarding the fresh and long-term durability and targeting the optimization of the mix designs using various potential raw materials are needed to facilitate the wide-scale use of these binders in building and other proposed applications.

6. Conclusions

Magnesium silicate hydrate (M-S-H) binders have been an attractive alternative cement by offering opportunities to decarbonize cement industry and novel applications due to their unique properties. In this review, we highlight the current knowledge, point out research gaps, and create a platform for the community to steer the research direction in this topic toward the common goal of mitigating the carbon footprint of cement industry.

Here are five key takeaways:

1) M-S-H is a nanocrystalline hydrated phyllosilicate whose structure highly depends on the Mg/Si ratio. The presence of aluminium in the precursor leads to M-(A-)S-H or hydrotalcite formation. One will need MgO- and silica-rich precursor to form the M-S-H binders. Often MgO and silica fume are used, and the formation of M-S-H phases shows a strong dependence on the physico-chemical properties of the precursors. M-S-H is the main strength-giving phase in the binders, reaching a similar range of compressive strength as Portland cement.

2) To decrease the production costs of M-S-H binders, other potential precursors (e.g., metakaolin, fly ash, rice husk ash, waste glass, slags, clay, olivine, etc.) need to investigate their role in the formation and performance of M-S-H binders. Some additives can improve M-S-H's reaction kinetics and formation, such as sodium hexametaphosphate and carbonate-containing admixtures like $NaHCO_3$, Na_2CO_3, hydromagnesite. These admixtures are known to influence the dissolution of $Mg(OH)_2$. Yet, a systematic approach and understanding to improve the reactivity of precursors, different additives, and their long-term effects are of increased interest.

3) M-S-H binders were found to have good dimensional stability and potentially lower oxygen and chloride permeability than Portland cement. Due to the low pH in these binders, there is a need to investigate the response of steel rebar used in these binders and the possibility of other types of rebar. Plus, we see a major gap for a better understanding of these binders' durability and long-term performance, such as stability in different chemical environments, e.g., sulfate and carbonation and assessment for risks due to the late reaction of unreacted MgO in the binders.

4) M-S-H binders offer unique applications both inside and outside the construction industry. The binders are suitable for disposing of wastes containing radioactive elements and heavy metals. Other potential applications include stabilizing cement for clay backfills, non-structural construction materials such as low-density thermal insulating boards and bricks, and components of refractory castable.

5) Prior to the mass application of the M-S-H binders, a comprehensive assessment of cost structure, feedstocks, and environmental footprint relating to the production of these binders is an important need. One major hurdle is the feedstock of MgO and SiO_2. MgO derived from calcinating $MgCO_3$ is known to be unsustainable due to its high CO_2 emissions as well as poor availability of high-quality feedstocks, while reactive SiO_2 is of high price. For these reasons, processes to tap into alternative MgO and SiO_2 feedstocks are being investigated, which can utilize abundant magnesium silicate rocks such as olivine, or desalination brines.

CRediT authorship contribution statement

Harisankar Sreenivasan: Conceptualization, Formal analysis, Investigation, Methodology, Writing – original draft, Writing – review & editing. **Ellina Bernard:** Conceptualization, Data curation, Formal analysis, Investigation, Methodology, Supervision, Validation, Visualization, Writing – original draft, Writing – review & editing. **Hellen S. Santos:** Data curation, Formal analysis, Investigation, Validation, Visualization, Writing – original draft, Writing – review & editing, Conceptualization, Methodology. **Hoang Nguyen:** Data curation, Formal analysis, Investigation, Methodology, Validation, Visualization, Writing – original draft, Writing – review & editing. **Samira Moukannaa:** Formal analysis, Validation, Writing – original draft, Writing – review & editing. **Adeolu Adediran:** Formal analysis, Writing – original draft, Writing – review & editing. **John L. Provis:** Conceptualization, Formal analysis, Investigation, Methodology, Supervision, Validation, Writing – original draft, Writing – review & editing. **Paivo Kinnunen:** Conceptualization, Data curation, Formal analysis, Funding acquisition, Investigation, Methodology, Resources, Supervision, Validation, Visualization, Writing – original draft, Writing – review & editing.

Declaration of competing interest

The authors declare that they have no known competing financial interests or personal relationships that could have appeared to influence the work reported in this paper.

Data availability

Data will be made available on request.

Acknowledgements

Appendix A

Table 1

M-S-H phases reported in the literature: precursors, admixtures, aggregates, molar ratios, w/b, curing conditions, Compressive strength, structure.

Precursors	Nature of M-S-H phase	Admixture, (wt% based on binder)	Aggregates or fibers (wt ratio based on binder	Molar ratios				w/b[a]	Curing conditions		Compressive strength (MPa)			Reference structure	Ref.
				Mg/Si	Ca/Si	Al/Si	Fe/Si		T (C)	RH (%)	3 days	7 days	28 days		
MgO, silica fume	Suspension	n.a.	n.a	0.4–1.7				45	20, 50	n.a	n.r	n.r	n.r	talc, lizardite antigorite, stevensite,	[39]
MgO, silica fume	Suspension	n.a.	n.a	0.57, 1.07				50	22	n.a.	n.r	n.r	n.r	talc	[40]
MgO, silica fume	Suspension	n.a.	n.a	0.7–1.6				45	20, 50, 70	n.r.	n.r	n.r	n.r	talc, antigorite,	[41]
MgO, silica fume	Suspension	n.a.	n.a	0.8, 1.2				45	20	n.r.	n.r	n.r	n.r	talc, stevensite, antigorite	[42]
MgO, CaO, silica fume	Suspension	n.a.	n.a	0–0.8	0–0.8			45	n.r.	c.p	n.r	n.r	n.r	talc	[81]
MgO, silica fume, metakaolin	Suspension	n.a	n.a	1.1, 1.7		0–0.2		45	20, 50, 70	n.r.	n.r	n.r	n.r	talc	[82]
Mg(OH)$_2$, silica fume	Paste	SHMP (0–5)	n.a	1.0	n.r	n.r.	n.r.	1	40	95	n.r.	0.6–1.3[b]	1.5–3.5[b]	lizardite	[5]
MgO, silica fume	Paste	SHMP (0–1.1)	n.a	1.0				0.4–0.8	20	98	n.r.	15.0-45.0[b]	25.0-70.0[b]	n.r	[1]
MgO, metakaolin	Paste	PCES (n.r.)	n.a	2.64–3.92[b]	0.06–0.08[b]	0.96–0.99[b]		0.5, 0.6	20	n.r.	n.r	n.r	n.r	n.r	[57]
Mg(OH)$_2$, microsilica	Paste	Na$_2$CO$_3$ (0–32.25)	n.a	1.04[b]				1	35	c.t	n.r	n.r	n.r	n.r	[68]
Mg(OH)$_2$, microsilica	Paste	NaHCO$_3$ (0–9.6)	n.a.	1.04[b]				1	35	c.t	n.r	n.r	n.r	n.r	[55]
Mg(NO$_3$)$_2$.6H$_2$O, Na$_2$SiO$_3$.5H$_2$O	Paste	n.a.	n.a.	0.67–1.00				n.r.	22, 85	c.r	n.r	n.r	n.r	n.r.	[77]
MgO, microsilica, rice husk ash	Paste	SHMP (1.0)	n.a.	1.49–1.78[b]	0.02[b]			0.55	28	95	n.r.	3.0-35.0[b]	10.0-40.0[b]	n.r	[58]
MgO, silica fume, metakaolin	Paste	PCE (n.r.)	n.a.	1.04–3.94[b]	0.01–0.06[b]	0.98–1.00[b]	0.01[b]	0.50	20	95	8.0-12.0[b]	10.0-23.0[b]	17.0-46.0[b]	n.r.	[64]
MgO, ceramic waste, glass waste	Paste	SHMP (1.0)	n.a.	1.66–2.19[b]	0.04–0.05[b]	0.01–0.36[b]	0–0.05[b]	0.35–0.37	20	95	3.0-20.0[b]	10.0-36.0[b]	15.0-47.0[b]	n.r.	[52]
MgO, silica fume, fly ash	Paste	SHMP (1.0)	n.a.	0.92–2.07[b]	0.01–0.37[b]	0–0.47[b]	0.01–0.14[b]	0.5	20	90	n.r.	0.10–2.40[b]	7.50–17.0[b]	n.r.	[59]
MgO, silica fume	Paste	SHMP (1.0), STMP (1.0), SOP(1.0)	n.a.	1.00	n.r.	n.r.	n.r.	0.80	n.r	n.r.	n.r	n.r	n.r	n.r	[66]
MgO, silica fume	Mortar	SHMP (2.0)	Chicken feathers (0–0.05), sand (1)	1.04[b]	n.a.	n.a	n.a.	0.5	20	95	n.r.	25.0–33.0[b]	33.0–47.0[b]	n.r	[156]
MgO, metakaolin	Mortar	PCE (n.r.), SVC5 (n.r.)	Stone dust (0.34–0.66[b])	1.42–2.51[b]	0.04–0.08[b]	0.79–0.89[b]		0.42–0.58	22	n.r	6.7–19.1	3.7–25.3	5.1–45.0	n.r.	[168]
MgO, silica fume, clay, metakaolin	Mortar	MgCO$_3$ (9.5–35.3[b]), PCE(3.0)	Quartz (0.10–0.35[b]), sand (1.0)	0.51–2.31[b]	0.02–0.09[b]	0.41–0.90[b]	0–0.02[b]	0.4	20	c.w	4.0–15.0[b]	6.0–25.0[b]	15.0–45.0[b]	n.r.	[60]

(continued on next page)

Table 1 (*continued*)

Precursors	Nature of M-S-H phase	Admixture, (wt% based on binder)	Aggregates or fibers (wt ratio based on binder)	Molar ratios				w/b[a]	Curing conditions		Compressive strength (MPa)			Reference structure	Ref.
				Mg/Si	Ca/Si	Al/Si	Fe/Si		T (C)	RH (%)	3 days	7 days	28 days		
MgO, microsilica	Mortar	SHMP(2.0), PCE (1.4)	PVA fibers (0.02[c])	1.48[b]	n.a	n.a.	n.a.	0.45	28	95	n.r	n.r	54.3	n.r.	[169]
MgO, silica fume	Mortar	n.a.	Fibers (0.11), limestone (0.33)	2.26[b]	n.a	n.a.	n.a.	0.53–0.60	25	c.w	n.r	n.r	9.03–9.23	n.r	[170]
MgO, silica fume	Mortar	MF (n.r.)	Cellulose fibers (n.r)	1.51–6.03[b]				0.5	30	95	n.r.	35.0-45.0[b]	50.0-70.0[b]	n.r	[140]
Olivine	Mortar	n.a.	Sand	1.95[b]	0.02[b]		0.20[b]	0.75	20	60	16.5	21.6	22	lizardite	[21]
MgO, microsilica	Mortar	SHMP(1.2), HM (1.0)	Coarse aggregates (1.5)	1.63[b]	0.05[b]	0.02[b]		0.46	30	95	n.r.	33.0-38.0[b]	60.0-43.0[b]	n.r	[69]
MgO, silica fume	Mortar	SHMP (1.0)	Sand (0.50–1.50[b])	1.00[b]				0.5–0.8	n.r.	c.b.	n.r	n.r	25.0–40.0[b]	n.r.	[141]
MgO, silica fume	Mortar	SVC5 (3)	quartz (0.11), sand (1.25–1.39) stone (2.00–2.22)	2.26[b]				0.4	20	c.w.	n.r	23.0-50.0[b]	40.00-63.0[b]	n.r.	[145]
MgO, Microsilica, metakaolin	Mortar	PCE	Standardized sand	1.5–2.5		0–3.2		0.9	23	98	5–11	8–17	10–21	n.r.	[138]
MgO, microsilica	Concrete	SHMP (2.0)	Coarse aggregates (0.6)	2.25	n.a	n.a.	n.a.	0.4	28 ± 2	95	n.r	n.r	76	n.r	[139]
MgO, metakaolin	Concrete	SVC5 (4.4–5.2), air-entrainment (180 ml/binder mass)	Fine+ coarse aggregates (2.5 & 1.7)	4.6	n.a	1	n.a	0.44–0.48	n.r.	n.r.	n.r.	n.r.	31–44	n.r.	[171]

Abbreviations used in the table: w/b- water to binder ratio, T-temperature, RH-relative humidity, UCS-unconfined compressive strength, HM-Hydromagnesite, SHMP-Sodium hexametaphosphate, STMP- sodium tri-metaphosphate, SOP- Sodium orthophosphate, PCE-Polycarboxylate ether, SVC5- Sika *ViscoCrete*-5-555, MF-Melflux 2651F, PVA-Polyvinyl alcohol, n.a. – not applicable, n.r. – not reported, c.b.-cured in closed box with excess of water to reduce sample drying, c.c-cured in polyethylene containers, c.t-cured in centrifuge tubes, c.r-cured in round bottom flask kept immersed in water bath.

[a] Water to binder ratio.
[b] Calculated based on provided data.
[c] Volume ratio.

References

[1] T. Zhang, L.J. Vandeperre, C.R. Cheeseman, Formation of magnesium silicate hydrate (M-S-H) cement pastes using sodium hexametaphosphate, Cem. Concr. Res. 65 (2014) 8–14, https://doi.org/10.1016/j.cemconres.2014.07.001.

[2] T. Zhang, T. Li, J. Zou, Y. Li, S. Zhi, Y. Jia, C.R. Cheeseman, Immobilization of radionuclide ^{133}Cs by magnesium silicate hydrate cement, Materials (Basel) 13 (2019) 146, https://doi.org/10.3390/ma13010146.

[3] M.R. Marsiske, C. Debus, F. Di Lorenzo, E. Bernard, S.V. Churakov, C. Ruiz-Agudo, Immobilization of (aqueous) cations in low pH M-S-H cement, Appl. Sci. 11 (2021) 2968, https://doi.org/10.3390/app11072968.

[4] D.R.M. Brew, F.P. Glasser, Synthesis and characterisation of magnesium silicate hydrate gels, Cem. Concr. Res. 35 (2005) 85–98, https://doi.org/10.1016/j.cemconres.2004.06.022.

[5] S.A. Walling, H. Kinoshita, S.A. Bernal, N.C. Collier, J.L. Provis, Structure and properties of binder gels formed in the system mg(OH)$_2$–SiO$_2$–H$_2$O for immobilisation of Magnox sludge, Dalton Trans. 44 (2015) 8126–8137, https://doi.org/10.1039/C5DT00877H.

[6] Magnesium-silicate-hydrate cements for encapsulating problematic aluminium containing wastes: Journal of Sustainable Cement-Based Materials: Vol 1, No 1–2, (n.d.). https://www.tandfonline.com/doi/abs/10.1080/21650373.2012.727322 (accessed May 21, 2023).

[7] J. Green, Calcination of precipitated mg(OH)$_2$ to active MgO in the production of refractory and chemical grade MgO, J. Mater. Sci. 18 (1983) 637–651, https://doi.org/10.1007/BF00745561.

[8] M.H. Bocanegra-Bernal, Agglomeration of magnesia powders precipitated from sea water and its effects on uniaxial compaction, Mater. Sci. Eng. A 333 (2002) 176–186, https://doi.org/10.1016/S0921-5093(01)01837-8.

[9] D. Barba, V. Brandani, G. Di Giacomo, P.U. Foscolo, Magnesium oxide production from concentrated brines, Desalination 33 (1980) 241–250, https://doi.org/10.1016/S0011-9164(00)88567-7.

[10] D. Hassan, Environmental Sustainability Assessment & Associated Experimental Investigations of Magnesia Production Routes, Ph.D., University of Cambridge, 2014. https://ethos.bl.uk/OrderDetails.do?uin=uk.bl.ethos.648574 (accessed May 21, 2023).

[11] H. Dong, C. Unluer, E.-H. Yang, A. Al-Tabbaa, Synthesis of reactive MgO from reject brine via the addition of NH$_4$OH, Hydrometallurgy 169 (2017) 165–172, https://doi.org/10.1016/j.hydromet.2017.01.010.

[12] S.H. Chu, E.H. Yang, C. Unluer, Chemical synthesis of magnesium oxide (MgO) from brine towards minimal energy consumption, Desalination 556 (2023) 116594, https://doi.org/10.1016/j.desal.2023.116594.

[13] Mining Valuable Minerals from Seawater: A Critical Review - Environmental Science: Water Research & Technology (RSC Publishing), (n.d.). https://pubs.rsc.org/en/content/articlelanding/2017/EW/C6EW00268D (accessed May 21, 2023).

[14] P. Badjatya, A.H. Akca, D.V. Fraga Alvarez, B. Chang, S. Ma, X. Pang, E. Wang, Q. van Hinsberg, D.V. Esposito, S. Kawashima, Carbon-negative cement manufacturing from seawater-derived magnesium feedstocks, Proc. Natl. Acad. Sci. 119 (2022) e2114680119, https://doi.org/10.1073/pnas.2114680119.

[15] H. Dong, E.-H. Yang, C. Unluer, F. Jin, A. Al-Tabbaa, Investigation of the properties of MgO recovered from reject brine obtained from desalination plants, J. Clean. Prod. 196 (2018) 100–108, https://doi.org/10.1016/j.jclepro.2018.06.032.

[16] N. Raza, W. Raza, S. Madeddu, H. Agbe, R.V. Kumar, K.-H. Kim, Synthesis and characterization of amorphous precipitated silica from alkaline dissolution of olivine, RSC Adv. 8 (2018) 32651–32658, https://doi.org/10.1039/C8RA06257A.

[17] A. Neubeck, N.T. Duc, H. Hellevang, C. Oze, D. Bastviken, Z. Bacsik, N.G. Holm, Olivine alteration and H$_2$ production in carbonate-rich, low temperature aqueous environments, Planet. Space Sci. 96 (2014) 51–61, https://doi.org/10.1016/j.pss.2014.02.014.

[18] A. Sanna, A. Lacinska, M. Styles, M.M. Maroto-Valer, Silicate rock dissolution by ammonium bisulphate for pH swing mineral CO$_2$ sequestration, Fuel Process. Technol. 120 (2014) 128–135, https://doi.org/10.1016/j.fuproc.2013.12.012.

[19] Q. Zhao, K. Liu, L. Sun, C. Liu, M. Jiang, H. Saxén, R. Zevenhoven, Towards carbon sequestration using stainless steel slag via phase modification and co-extraction of calcium and magnesium, Process Saf. Environ. Prot. 133 (2020) 73–81, https://doi.org/10.1016/j.psep.2019.11.004.

[20] S.A. Walling, J.L. Provis, Magnesia-based cements: a journey of 150 years, and cements for the future? Chem. Rev. 116 (2016) 4170–4204, https://doi.org/10.1021/acs.chemrev.5b00463.

[21] S. Allan Nye, S. Vineet, O. Christopher, S. Barnaby, C. Chris, Use of olivine for the production of MgO-SiO$_2$ binders, Frontiers, Built Environ. 7 (2021) 76, https://doi.org/10.3389/fbuil.2021.640243.

[22] Development of magnesium silicate hydrate binder systems., (n.d.). https://ir.canterbury.ac.nz/handle/10092/17557 (accessed January 5, 2022).

[23] Cement Cummings, US402511A. https://patents.google.com/patent/US402511A/en, 1889. (Accessed 3 January 2022).

[24] A. Gillies, W. Gillies, Process for the Manufacture of Artificial Stone, US1038115A, 1912. https://patents.google.com/patent/US1038115A/en (accessed January 3, 2022).

[25] J. Steiger, Manufacture of Cement, US627884A. https://patents.google.com/patent/US627884A/en, 1899. (Accessed 3 January 2022).

[26] Process of treating asbestos-bearing rock, US1317852A. https://patents.google.com/patent/US1317852A/en, 1919. (Accessed 3 January 2022).

[27] H.C. Michell, Manufacture of Non-conducting Coverings, Blocks, and Slabs, US774946A. https://patents.google.com/patent/US774946/en, 1904. (Accessed 3 January 2022).

[28] W.F. Cole, A crystalline hydrated magnesium silicate formed in the breakdown of a concrete sea-wall, Nature 171 (1953) 354–355, https://doi.org/10.1038/171354a0.

[29] D. Bonen, Composition and appearance of magnesium silicate hydrate and its relation to deterioration of cement-based materials, J. Am. Ceram. Soc. 75 (1992) 2904–2906, https://doi.org/10.1111/j.1151-2916.1992.tb05530.x.

[30] D.R.M. Brew, F.P. Glasser, Reactions of sulphate-resistant Portland cement and its blends with silica fume and aqueous magnesium sulphate, Adv. Cem. Res. 14 (2002) 101–111, https://doi.org/10.1680/adcr.2002.14.3.101.

[31] M. Santhanam, M.D. Cohen, J. Olek, Mechanism of sulfate attack: a fresh look: part 2, Proposed mechanisms, Cement and Concrete Research 33 (2003) 341–346, https://doi.org/10.1016/S0008-8846(02)00958-4.

[32] R.S. Gollop, H.F.W. Taylor, Microstructural and microanalytical studies of sulfate attack. I. Ordinary Portland cement paste, Cem. Concr. Res. 22 (1992) 1027–1038, https://doi.org/10.1016/0008-8846(92)90033-R.

[33] B. Fleury, N. Godon, A. Ayral, S. Gin, SON68 glass dissolution driven by magnesium silicate precipitation, J. Nucl. Mater. 442 (2013) 17–28, https://doi.org/10.1016/j.jnucmat.2013.08.029.

[34] N.J. Tosca, F.A. Macdonald, J.V. Strauss, D.T. Johnston, A.H. Knoll, Sedimentary talc in Neoproterozoic carbonate successions, Earth Planet. Sci. Lett. 306 (2011) 11–22, https://doi.org/10.1016/j.epsl.2011.03.041.

[35] A. Dauzeres, P. Le Bescop, P. Sardini, C., Cau Dit Coumes, Physico-chemical investigation of clayey/cement-based materials interaction in the context of geological waste disposal: experimental approach and results, Cem. Concr. Res. 40 (2010) 1327–1340, https://doi.org/10.1016/j.cemconres.2010.03.015.

[36] S. Carroll, W. McNab, S. Torres, M. Singleton, P. Zhao, Wellbore integrity in carbon sequestration environments: 1. Experimental study of cement–sandstone/shale–brine–CO$_2$, Energy Procedia 4 (2011) 5186–5194, https://doi.org/10.1016/j.egypro.2011.02.496.

[37] J. Szczerba, R. Prorok, E. Śnieżek, D. Madej, K. Maślona, Influence of time and temperature on ageing and phases synthesis in the MgO–SiO2–H2O system, Thermochim. Acta 567 (2013) 57–64, https://doi.org/10.1016/j.tca.2013.01.018.

[38] J. Wei, Q. Yu, W. Zhang, H. Zhang, Reaction products of MgO and microsilica cementitious materials at different temperatures, J. Wuhan Univ. Technol.-Mat. Sci. Edit. 26 (2011) 745–748, https://doi.org/10.1007/s11595-011-0304-3.

[39] D. Nied, K. Enemark-Rasmussen, E. L'Hopital, J. Skibsted, B. Lothenbach, Properties of magnesium silicate hydrates (M-S-H), Cem. Concr. Res. 79 (2016) 323–332, https://doi.org/10.1016/j.cemconres.2015.10.003.

[40] C. Roosz, S. Grangeon, P. Blanc, V. Montouillout, B. Lothenbach, P. Henocq, E. Giffaut, P. Vieillard, S. Gaboreau, Crystal structure of magnesium silicate hydrates (M-S-H): the relation with 2:1 mg–Si phyllosilicates, Cem. Concr. Res. 73 (2015) 228–237, https://doi.org/10.1016/j.cemconres.2015.03.014.

[41] E. Bernard, B. Lothenbach, D. Rentsch, I. Pochard, A. Dauzères, Formation of magnesium silicate hydrates (M-S-H), Physics and Chemistry of the Earth, Parts A/B/C 99 (2017) 142–157, https://doi.org/10.1016/j.pce.2017.02.005.

[42] E. Bernard, B. Lothenbach, C. Chlique, M. Wyrzykowski, A. Dauzères, I. Pochard, C. Cau-Dit-Coumes, Characterization of magnesium silicate hydrate (M-S-H), Cem. Concr. Res. 116 (2019) 309–330, https://doi.org/10.1016/j.cemconres.2018.09.007.

[43] T. Zhang, Luc.J. Vandeperre, C.R. Cheeseman, Magnesium-silicate-hydrate cements for encapsulating problematic aluminium containing wastes, Journal of Sustainable Cement-Based Materials 1 (2012) 34–45. doi:https://doi.org/10.1080/21650373.2012.727322.

[44] E. Bernard, Research progress on magnesium silicate hydrate phases and future opportunities, RILEM Technical Letters 7 (2022) 47–57, https://doi.org/10.21809/rilemtechlett.2022.162.

[45] H.A. Abdel-Gawwad, S. Abd El-Aleem, A. Zayed, Stabilization of hazardous lead glass sludge using reactive magnesia via the fabrication of lightweight building bricks, J. Hazard. Mater. 403 (2021) 124017, https://doi.org/10.1016/j.jhazmat.2020.124017.

[46] L. Wang, L. Chen, D.-W. Cho, D.C.W. Tsang, J. Yang, D. Hou, K. Baek, H.W. Kua, C.-S. Poon, Novel synergy of Si-rich minerals and reactive MgO for stabilisation/solidification of contaminated sediment, J. Hazard. Mater. 365 (2019) 695–706, https://doi.org/10.1016/j.jhazmat.2018.11.067.

[47] B. Panda, C. Sonat, E.-H. Yang, M.J. Tan, C. Unluer, Use of magnesium-silicate-hydrate (M-S-H) cement mixes in 3D printing applications, Cement and Concrete Composites 117 (2021) 103901, https://doi.org/10.1016/j.cemconcomp.2020.103901.

[48] H.A. Abdel-Gawwad, H.S. Hassan, S.R. Vásquez-García, I. Israde-Alcántara, Y.-C. Ding, M.A. Martinez-Cinco, S. Abd El-Aleem, H.M. Khater, T.A. Tawfik, I.M. El-Kattan, Towards a clean environment: the potential application of eco-friendly magnesia-silicate cement in CO2 sequestration, J. Clean. Prod. 252 (2020) 119875, https://doi.org/10.1016/j.jclepro.2019.119875.

[49] P. Assawasaengrat, P. Jintanavasan, P. Kitchaiya, Adsorption of FFA, soap and glycerine in biodiesel using magnesium silicate, chemical, Eng. Trans. 43 (2015) 1135–1140, https://doi.org/10.3303/CET1543190.

[50] R. Salomão, V.C. Pandolfelli, Citric acid as anti-hydration additive for magnesia containing refractory castables, Ceram. Int. 37 (2011) 1839–1842, https://doi.org/10.1016/j.ceramint.2011.03.050.

[51] T. dos Santos, F.G. Pinola, A.P. Luz, C. Pagliosa, V.C. Pandolfelli, Al$_2$O$_3$-MgO refractory castables with enhanced explosion resistance due to in situ formation

of phases with lamellar structure, Ceram. Int. 44 (2018) 8048–8056, https://doi.org/10.1016/j.ceramint.2018.01.246.

[52] H.A. Abdel-Gawwad, S. Abd El-Aleem, A.A. Amer, H. El-Didamony, M.A. Arif, Combined impact of silicate-amorphicity and MgO-reactivity on the performance of mg-silicate cement, Construct. Build Mater. 189 (2018) 78–85, https://doi.org/10.1016/j.conbuildmat.2018.08.171.

[53] R. Hay, K. Celik, Hydration, carbonation, strength development and corrosion resistance of reactive MgO cement-based composites, Cem. Concr. Res. 128 (2020) 105941, https://doi.org/10.1016/j.cemconres.2019.105941.

[54] F. Jin, A. Al-Tabbaa, Thermogravimetric study on the hydration of reactive magnesia and silica mixture at room temperature, Thermochimica Acta 566 (2013) 162–168, https://doi.org/10.1016/j.tca.2013.05.036.

[55] H. Zhao, T. Hanein, N. Li, A. Alotaibi, A. Li, S. Walling, H. Kinoshita, Acceleration of M-S-H gel formation through the addition of alkali carbonates, Proceedings of the 15th International Congress on the Chemistry of Cement (ICCC 2019) (2019). doi:10/1/paper%20605%20%282%29.pdf.

[56] C. Dewitte, A. Bertron, M. Neji, L. Lacarrière, A. Dauzères, Chemical and microstructural properties of designed cohesive M-S-H pastes, Materials 15 (2022) 547, https://doi.org/10.3390/ma15020547.

[57] V. Shah, Y. Dhandapani, A. Scott, Pore structure characteristics of MgO–SiO$_2$ binder, J. Am. Ceram. Soc. 104 (2021) 6002–6014, https://doi.org/10.1111/jace.17971.

[58] C. Sonat, C. Unluer, Development of magnesium-silicate-hydrate (M-S-H) cement with rice husk ash, J. Clean. Prod. 211 (2019) 787–803, https://doi.org/10.1016/j.jclepro.2018.11.246.

[59] T.T. Zhang, Y.N. Du, Y.J. Sun, Z.M. He, Z.L. Wu, Development of magnesium-silicate-hydrate cement by pulverized fuel ash, Key Eng. Mater. 709 (2016) 61–65, https://doi.org/10.4028/www.scientific.net/KEM.709.61.

[60] V. Shah, A. Scott, Use of kaolinite clays in development of a low carbon MgO-clay binder system, Cem. Concr. Res. 144 (2021) 106422, https://doi.org/10.1016/j.cemconres.2021.106422.

[61] L.J. Vandeperre, M. Liska, A. Al-Tabbaa, Hydration and mechanical properties of magnesia, pulverized fuel ash, and Portland cement blends, Journal of Materials in Civil Engineering 20 (2008) 375–383, https://doi.org/10.1061/(ASCE)0899-1561(2008)20:5(375).

[62] R. Snellings, Solution-controlled dissolution of supplementary cementitious material glasses at pH 13: the effect of solution composition on glass dissolution rates, J. Am. Ceram. Soc. 96 (2013) 2467–2475, https://doi.org/10.1111/jace.12480.

[63] Y. Jia, B. Wang, Z. Wu, T. Zhang, Effect of CaO on the reaction process of MgO–SiO$_2$-H$_2$O cement pastes, Mater. Lett. 192 (2017) 48–51, https://doi.org/10.1016/j.matlet.2017.01.072.

[64] V. Shah, A. Scott, Hydration and microstructural characteristics of MgO in the presence of metakaolin and silica fume, Cement and Concrete Composites 121 (2021) 104068, https://doi.org/10.1016/j.cemconcomp.2021.104068.

[65] Y. Jia, B. Wang, Z. Wu, J. Han, T. Zhang, L.J. Vandeperre, C.R. Cheeseman, Role of sodium hexametaphosphate in MgO/SiO$_2$ cement pastes, Cem. Concr. Res. 89 (2016) 63–71, https://doi.org/10.1016/j.cemconres.2016.08.003.

[66] M. Tonelli, F. Martini, A. Milanesi, L. Calucci, M. Geppi, S. Borsacchi, F. Ridi, Effect of phosphate additives on the hydration process of magnesium silicate cements, J Therm Anal Calorim 138 (2019) 3311–3321, https://doi.org/10.1007/s10973-019-08847-9.

[67] H.M. Tran, A. Scott, Strength and workability of magnesium silicate hydrate binder systems, Construct. Build Mater. 131 (2017) 526–535, https://doi.org/10.1016/j.conbuildmat.2016.11.109.

[68] H. Zhao, T. Hanein, H. Kinoshita, The Effect of Sodium Carbonate on the Formation of Magnesium Silicate Hydrate, 40th Cement and Concrete Science Conference Proceedings. https://eprints.whiterose.ac.uk/162983/, 2020. (Accessed 25 January 2022).

[69] G.V.P. Bhagath Singh, C. Sonat, E.H. Yang, C. Unluer, Performance of MgO and MgO–SiO$_2$ systems containing seeds under different curing conditions, Cement and Concrete Composites 108 (2020) 103543, https://doi.org/10.1016/j.cemconcomp.2020.103543.

[70] E. Bernard, H. Nguyen, S. Kawashima, B. Lothenbach, H. Manzano, J. Provis, A. Scott, C. Unluer, F. Winnefeld, P. Kinnunen, MgO-Based Cements – Current Status and Opportunities, RILEM Technical Letters, RILEM Technical Letters, (2023, Accepted)., n.d.

[71] T. Manfredini, G.C. Pellacani, P. Pozzi, A.B. Corradi, Monomeric and oligomeric phosphates as deflocculants of concentrated aqueous clay suspensions, Applied Clay Science 5 (1990) 193–201, https://doi.org/10.1016/0169-1317(90)90009-E.

[72] O.M. Smirnova, Low-clinker cements with low water demand, J. Mater. Civ. Eng. 32 (2020) 06020008, https://doi.org/10.1061/(ASCE)MT.1943-5533.0003241.

[73] K.H. Khayat, A. Yahia, M. Sayed, Effect of supplementary cementitious materials on rheological properties, bleeding, and strength of structural grout, MJ 105 (2008) 585–593, https://doi.org/10.14359/20200.

[74] T.C. Powers, T.L. Brownyard, Studies of the physical properties of hardened Portland cement paste, JP 43 (1946) 249–336, https://doi.org/10.14359/15301.

[75] Z. Li, T. Zhang, J. Hu, Y. Tang, Y. Niu, J. Wei, Q. Yu, Characterization of reaction products and reaction process of MgO–SiO2–H2O system at room temperature, Construct. Build Mater. 61 (2014) 252–259, https://doi.org/10.1016/j.conbuildmat.2014.03.004.

[76] R. Salomão, V.C. Pandolfelli, Efeito da adição de microssílica na hidratação de óxido de magnésio em concretos refratários, Cerâmica 54 (2008) 43–48, https://doi.org/10.1590/S0366-69132008000100007.

[77] D.R.M. Brew, F.P. Glasser, Synthesis and characterisation of magnesium silicate hydrate gels, Cement Concrete Res. 35 (2005) 85–98, https://doi.org/10.1016/j.cemconres.2004.06.022.

[78] M.R. Marsiske, R. Köser, B. Bäumle, C. Ruiz-Agudo, Uncovering the early stages of magnesium silicate hydrate formation: a nonclassical multistep pathway, ACS Appl. Eng. Mater. 1 (2023) 696–707, https://doi.org/10.1021/acsaenm.2c00258.

[79] T. Zhang, C.R. Cheeseman, L.J. Vandeperre, Development of low pH cement systems forming magnesium silicate hydrate (M-S-H), Cem. Concr. Res. 41 (2011) 439–442, https://doi.org/10.1016/j.cemconres.2011.01.016.

[80] E. Bernard, B. Lothenbach, D. Rentsch, A. German, F. Winnefeld, Effect of carbonates on the formation of magnesium silicate hydrates, Mater Struct 55 (2022) 183, https://doi.org/10.1617/s11527-022-02018-3.

[81] B. Lothenbach, D. Nied, E. L'Hôpital, G. Achiedo, A. Dauzères, Magnesium and calcium silicate hydrates, Cem. Concr. Res. 77 (2015) 60–68, https://doi.org/10.1016/j.cemconres.2015.06.007.

[82] E. Bernard, B. Lothenbach, C. Cau-Dit-Coumes, I. Pochard, D. Rentsch, Aluminum incorporation into magnesium silicate hydrate (M-S-H), Cem. Concr. Res. 128 (2020) 105931, https://doi.org/10.1016/j.cemconres.2019.105931.

[83] M. Shimbashi, S. Yokoyama, Y. Watanabe, T. Sato, T. Otake, R. Kikuchi, M. Yamakawa, N. Fujii, Formation of natural silicate hydrates by the interaction of alkaline seepage and sediments derived from serpentinized ultramafic rocks at Narra, Palawan, the Philippines, Minerals 10 (2020) 719, https://doi.org/10.3390/min10080719.

[84] K. De Weerdt, H. Justnes, The effect of sea water on the phase assemblage of hydrated cement paste, Cement and Concrete Composites 55 (2015) 215–222, https://doi.org/10.1016/j.cemconcomp.2014.09.006.

[85] A. Dauzeres, G. Achiedo, D. Nied, E. Bernard, S. Alahrache, B. Lothenbach, Magnesium perturbation in low-pH concretes placed in clayey environment—solid characterizations and modeling, Cem. Concr. Res. 79 (2016) 137–150, https://doi.org/10.1016/j.cemconres.2015.09.002.

[86] A. Pedone, F. Palazzetti, V. Barone, Models of aged magnesium–silicate–hydrate cements based on the Lizardite and talc crystals: a periodic DFT-GIPAW investigation, J. Phys. Chem. C 121 (2017) 7319–7330, https://doi.org/10.1021/acs.jpcc.7b00708.

[87] Strukturverfeinerung am Talk Mg$_3$[(OH)$_2$Si$_4$O$_{10}$], Zeitschrift Für Kristallographie, Crystalline Materials 156 (1981) 177–186, https://doi.org/10.1524/zkri.1981.156.3-4.177.

[88] B. Perdikatsis, H. Burzlaff, eds., Strukturverfeinerung am Talk Mg$_3$[(OH)$_2$Si$_4$O$_{10}$], Zeitschrift Für Kristallographie - Crystalline Materials 156 (1981) 177–186. doi: https://doi.org/10.1524/zkri.1981.156.3-4.177.

[89] Clay-Containing Polymer Nanocomposites, Volumes 1 and 2: Polymer News: Vol 30, No 4, (n.d.). https://www.tandfonline.com/doi/abs/10.1080/00323910500458989 (accessed July 9, 2023).

[90] F. Bergaya, B.K.G. Theng, G. Legaly, Handbook of Clay Sciences, 1st ed, Elsevier Ltd., 2006, https://doi.org/10.1016/S1572-4352(05)01001-9.

[91] H.S. Santos, Halogen hectorites: Smectites designed to luminesce, PhD thesis, Turku University, https://urn.fi/URN:ISBN:978-951-29-7070-4.

[92] M. Tonelli, F. Martini, L. Calucci, E. Fratini, M. Geppi, F. Ridi, S. Borsacchi, P. Baglioni, Structural characterization of magnesium silicate hydrate: towards the design of eco-sustainable cements, Dalton Trans. 45 (2016) 3294–3304, https://doi.org/10.1039/C5DT03545G.

[93] M. Simoni, C.L. Woo, H. Zhao, D. Iuga, P. Svora, T. Hanein, H. Kinoshita, B. Walkley, Reaction mechanisms, kinetics, and nanostructural evolution of magnesium silicate hydrate (M-S-H) gels, Cem. Concr. Res. 174 (2023) 107295, https://doi.org/10.1016/j.cemconres.2023.107295.

[94] E. Bernard, Magnesium silicate hydrate (M-S-H) characterization: temperature, calcium, aluminum and alkali, Université de Bourgogne Franche-Comté, 2017. https://www.dora.lib4ri.ch/empa/islandora/object/empa%3A15957/. (Accessed 7 January 2022).

[95] K.J.D. MacKenzie, R.H. Meinhold, Thermal reactions of chrysotile revisited: a ^{29}Si and ^{25}Mg MAS NMR study, Am. Mineral. 79 (1994) 43–50.

[96] J.-B.D. de la Caillerie, J.J. Fripiat, A reassessment of the ^{29}Si MAS-NMR spectra of sepiolite and aluminated sepiolite, Clay Miner. 29 (1994) 313–318, https://doi.org/10.1180/claymin.1994.029.3.02.

[97] M.A. Aramendía, V. Borau, C. Jiménez, J.M. Marinas, J.R. Ruiz, Characterization of Spanish sepiolites by high-resolution solid-state NMR, Solid State Nucl. Magn. Reson. 8 (1997) 251–256, https://doi.org/10.1016/s0926-2040(97)00009-x.

[98] M. Eir, W. Kuang, G. Facey, C. Detellier, Solid-state nuclear magnetic resonance study of sepiolite and partially dehydrated sepiolite, Clay Clay Miner. 50 (2002) 240–247, https://doi.org/10.1346/000986002760832838.

[99] B. Rhouta, H. Kaddami, J. Elbarqy, M. Amjoud, I. Daoudi, F. Maury, F. Senocq, A. Maazouz, F. Gerard, Elucidating the crystal-chemistry of Jbel Rhassoul stevensite (Morocco) by advanced analytical techniques, Clay Miner. 43 (2008) 393–403, https://doi.org/10.1180/claymin.2008.043.3.05.

[100] K. Chabrol, M. Gressier, N. Pebere, M.-J. Menu, F. Martin, J.-P. Bonino, C. Marichal, J. Brendle, Functionalization of synthetic talc-like phyllosilicates by alkoxyorganosilane grafting, J. Mater. Chem. 20 (2010) 9695–9706, https://doi.org/10.1039/C0JM01276A.

[101] A. Dumas, F. Martin, C. Le Roux, P. Micoud, S. Petit, E. Ferrage, J. Brendlé, O. Grauby, M. Greenhill-Hooper, Phyllosilicates synthesis: a way of accessing edges contributions in NMR and FTIR spectroscopies, Example of synthetic talc, Phys Chem Minerals 40 (2013) 361–373, https://doi.org/10.1007/s00269-013-0577-5.

[102] L. Lin, D. Cornu, M. Mounir Daou, C. Domingos, V. Herledan, G. Krafft, G. Laugel, Y. Millot, H. Lauron-Pernot, Role of Water on the Activity of Magnesium Silicate

for Transesterification Reactions (2017), https://doi.org/10.1002/cctc.201700139.

[103] W.-S. Chiang, G. Ferraro, E. Fratini, F. Ridi, Y.-Q. Yeh, U.-S. Jeng, S.-H. Chen, P. Baglioni, Multiscale structure of calcium- and magnesium-silicate-hydrate gels, J. Mater. Chem. A 2 (2014) 12991–12998, https://doi.org/10.1039/C4TA02479F.

[104] F. Jin, A. Al-Tabbaa, Strength and hydration products of reactive MgO–silica pastes, Cement and Concrete Composites 52 (2014) 27–33, https://doi.org/10.1016/j.cemconcomp.2014.04.003.

[105] R.L. Frost, O.B. Locos, H. Ruan, J.T. Kloprogge, Near-infrared and mid-infrared spectroscopic study of sepiolites and palygorskites, Vib. Spectrosc. 27 (2001) 1–13, https://doi.org/10.1016/S0924-2031(01)00110-2.

[106] R.L. Frost, J.T. Kloprogge, Infrared emission spectroscopic study of brucite, Spectrochim. Acta A Mol. Biomol. Spectrosc. 55 (1999) 2195–2205, https://doi.org/10.1016/S1386-1425(99)00016-5.

[107] T. Mitsuda, H. Taguchi, Formation of magnesium silicate hydrate and its crystallization to talc, Cem. Concr. Res. 7 (1977) 223–230, https://doi.org/10.1016/0008-8846(77)90083-7.

[108] E. Bernard, B. Lothenbach, I. Pochard, C. Cau-Dit-Coumes, Alkali binding by magnesium silicate hydrates, J. Am. Ceram. Soc. 102 (2019) 6322–6336, https://doi.org/10.1111/jace.16494.

[109] J.M. Skluzacek, M. Isabel Tejedor, M.A. Anderson, An iron-modified silica nanofiltration membrane: effect of solution composition on salt rejection, Microporous Mesoporous Mater. 94 (2006) 288–294, https://doi.org/10.1016/j.micromeso.2006.03.043.

[110] M.C. Bruzzoniti, R.M. De Carlo, S. Fiorilli, B. Onida, C. Sarzanini, Functionalized SBA-15 mesoporous silica in ion chromatography of alkali, alkaline earths, ammonium and transition metal ions, J. Chromatogr. A 1216 (2009) 5540–5547, https://doi.org/10.1016/j.chroma.2009.05.052.

[111] J.M. Cases, I. Berend, G. Besson, M. Francois, J.P. Uriot, F. Thomas, J.E. Poirier, Mechanism of adsorption and desorption of water vapor by homoionic montmorillonite. 1. The sodium-exchanged form, Langmuir 8 (1992) 2730–2739, https://doi.org/10.1021/la00047a025.

[112] C. Sangwichien, G.L. Aranovich, M.D. Donohue, Density functional theory predictions of adsorption isotherms with hysteresis loops, Colloids Surf. A Physicochem. Eng. Asp. 206 (2002) 313–320, https://doi.org/10.1016/S0927-7757(02)00048-1.

[113] S. Chevalier, R. Franck, J.F. Lambert, D. Barthomeuf, H. Suquet, Characterization of the porous structure and cracking activity of Al-pillared saponites, Appl. Catal. Gen. 110 (1994) 153–165.

[114] T. Zhang, Z. He, Z. Wu, J. Han, Chloride Ion Penetration Resistance and Pore Structure of Magnesium Silicate Hydrate (M-S-H) Mortars, Atlantis Press, in, 2018, pp. 158–161, https://doi.org/10.2991/icmea-17.2018.36.

[115] D.A. Kulik, Improving the structural consistency of C-S-H solid solution thermodynamic models, Cem. Concr. Res. 41 (2011) 477–495, https://doi.org/10.1016/j.cemconres.2011.01.012.

[116] C. Roosz, P. Vieillard, P. Blanc, S. Gaboreau, H. Gailhanou, D. Braithwaite, V. Montouillout, R. Denoyel, P. Henocq, P. Madé, Thermodynamic properties of C-S-H, C-A-S-H and M-S-H phases: results from direct measurements and predictive modelling, Appl. Geochem. 92 (2018) 140–156, https://doi.org/10.1016/j.apgeochem.2018.03.004.

[117] Y. Tardy, J. Duplay, A method of estimateng the Gibbs free energies of formation of hydrated and dehydrated clay minerals, Geochim. Cosmochim. Acta 56 (1992) 3007–3029, https://doi.org/10.1016/0016-7037(92)90287-S.

[118] H.C. Helgeson, J.Delany, H.W. Nesbitt, D.K. Bird, Summary and critique of the thermodynamic properties of rock-forming minerals, http://www.dewcommunity.org/uploads/4/1/7/6/41765907/helgeson_et_al_1978.pdf.

[119] T.J.B. Holland, R. Powell, An internally consistent thermodynamic data set for phases of petrological interest, J. Metam. Geol. 16 (1998) 309–343, https://doi.org/10.1111/j.1525-1314.1998.00140.x.

[120] E. Melekhova, M.W. Schmidt, P. Ulmer, E. Guggenbühl, The reaction talc + forsterite = enstatite + H_2O revisited: application of conventional and novel experimental techniques and derivation of revised thermodynamic properties, Am. Mineral. 91 (2006) 1081–1088, https://doi.org/10.2138/am.2006.2065.

[121] E. Bernard, B. Lothenbach, C. Cau-Dit-Coumes, C. Chlique, A. Dauzères, I. Pochard, Magnesium and calcium silicate hydrates, part I: investigation of the possible magnesium incorporation in calcium silicate hydrate (C-S-H) and of the calcium in magnesium silicate hydrate (M-S-H), Appl. Geochem. 89 (2018) 229–242, https://doi.org/10.1016/j.apgeochem.2017.12.005.

[122] E. Bernard, A. Dauzères, B. Lothenbach, Magnesium and calcium silicate hydrates, part II: mg-exchange at the interface "low-pH" cement and magnesium environment studied in a C-S-H and M-S-H model system, Appl. Geochem. 89 (2018) 210–218, https://doi.org/10.1016/j.apgeochem.2017.12.006.

[123] B. Lothenbach, D.A. Kulik, T. Matschei, M. Balonis, L. Baquerizo, B. Dilnesa, G. D. Miron, R.J. Myers, Cemdata18: a chemical thermodynamic database for hydrated Portland cements and alkali-activated materials, Cem. Concr. Res. 115 (2019) 472–506, https://doi.org/10.1016/j.cemconres.2018.04.018.

[124] Phase formation and evolution in mg(OH)2–zeolite cements | Ind. Eng. Chem. Res., (n.d.). https://pubs.acs.org/doi/10.1021/acs.iecr.7b04201 (accessed July 9, 2023).

[125] L. de Ruiter, H. Austrheim, Formation of magnesium silicate hydrate cement in nature, J. Geol. Soc. London 175 (2018) 308–320, https://doi.org/10.1144/jgs2017-089.

[126] Standard Absolute Entropy, , Values from Volume or Density. 1. Inorganic Materials | Inorganic Chemistry, (n.d.). https://pubs.acs.org/doi/10.1021/ic030219p (accessed July 10, 2023).

[127] L. Glasser, Ambient heat capacities and entropies of ionic solids: a unique view using the Debye equation, Inorg. Chem. 52 (2013) 6590–6594, https://doi.org/10.1021/ic400617u.

[128] J. Leitner, P. Voňka, D. Sedmidubský, P. Svoboda, Application of Neumann–Kopp rule for the estimation of heat capacity of mixed oxides, Thermochimica Acta 497 (2010) 7–13. doi:https://doi.org/10.1016/j.tca.2009.08.002.

[129] H. Kopp, T. Graham III, Investigations of the specific heat of solid bodies, Philos. Trans. R. Soc. Lond. 155 (1997) 71–202, https://doi.org/10.1098/rstl.1865.0003.

[130] E. Bernard, B. Lothenbach, D. Rentsch, I. Pochard, A. Dauzères, Formation of magnesium silicate hydrates (M-S-H), Physics and Chemistry of the Earth, Parts A/B/C 99 (2017) 142–157, https://doi.org/10.1016/j.pce.2017.02.005.

[131] K. De Weerdt, B. Lothenbach, M.R. Geiker, Comparing chloride ingress from seawater and NaCl solution in Portland cement mortar, Cem. Concr. Res. 115 (2019) 80–89, https://doi.org/10.1016/j.cemconres.2018.09.014.

[132] K. De Weerdt, E. Bernard, W. Kunther, M.T. Pedersen, B. Lothenbach, Phase changes in cementitious materials exposed to saline solutions, Cem. Concr. Res. 165 (2023) 107071, https://doi.org/10.1016/j.cemconres.2022.107071.

[133] X. Ke, S.A. Bernal, J.L. Provis, B. Lothenbach, Thermodynamic modelling of phase evolution in alkali-activated slag cements exposed to carbon dioxide, Cem. Concr. Res. 136 (2020) 106158, https://doi.org/10.1016/j.cemconres.2020.106158.

[134] F. Winnefeld, E. Epifania, F. Montagnaro, E.M. Gartner, Further studies of the hydration of MgO-hydromagnesite blends, Cem. Concr. Res. 126 (2019) 105912, https://doi.org/10.1016/j.cemconres.2019.105912.

[135] J. Tanaka, J. Kawano, T. Nagai, H. Teng, Transformation process of amorphous magnesium carbonate in aqueous solution, J. Mineral. Petrol. Sci. 114 (2019) 105–109, https://doi.org/10.2465/jmps.181119b.

[136] H. Nguyen, H. Santos, H. Sreenivasan, W. Kunther, V. Carvelli, M. Illikainen, P. Kinnunen, On the carbonation of brucite: effects of mg-acetate on the precipitation of hydrated magnesium carbonates in aqueous environment, Cem. Concr. Res. 153 (2022) 106696, https://doi.org/10.1016/j.cemconres.2021.106696.

[137] E. Bernard, W.J. Zucha, B. Lothenbach, U. Mäder, Stability of hydrotalcite (mg-Al layered double hydroxide) in presence of different anions, Cem. Concr. Res. 152 (2022) 106674, https://doi.org/10.1016/j.cemconres.2021.106674.

[138] E. Bernard, B. Lothenbach, A. German, D. Rentsch, F. Winnefeld, Effect of aluminate and carbonate in magnesia silicate cement, Cem. Concr. Compos. 139 (2023) 105010, https://doi.org/10.1016/j.cemconcomp.2023.105010.

[139] C. Sonat, W.W. Teo, C. Unluer, Performance and microstructure of MgO-SiO2 concrete under different environments, Construct. Build Mater. 184 (2018) 549–564, https://doi.org/10.1016/j.conbuildmat.2018.07.032.

[140] G. Mármol, H. Savastano, M.M. Tashima, J.L. Provis, Optimization of the MgOSiO2 binding system for fiber-cement production with cellulosic reinforcing elements, Mater. Des. 105 (2016) 251–261, https://doi.org/10.1016/j.matdes.2016.05.064.

[141] T. Zhang, X. Liang, C. Li, M. Lorin, Y. Li, L.J. Vandeperre, C.R. Cheeseman, Control of drying shrinkage in magnesium silicate hydrate (m-s-h) gel mortars, Cem. Concr. Res. 88 (2016) 36–42, https://doi.org/10.1016/j.cemconres.2016.05.011.

[142] R.J. Flatt, G.W. Scherer, Thermodynamics of crystallization stresses in DEF, Cem. Concr. Res. 38 (2008) 325–336, https://doi.org/10.1016/j.cemconres.2007.10.002.

[143] H. Nguyen, V. Carvelli, W. Kunther, M. Illikainen, P. Kinnunen, Phase evolution and mechanical performance of an ettringite-based binder during hydrothermal aging, Cem. Concr. Res. 143 (2021) 106403, https://doi.org/10.1016/j.cemconres.2021.106403.

[144] H. Kabir, R.D. Hooton, N.J. Popoff, Evaluation of cement soundness using the ASTM C151 autoclave expansion test, Cem. Concr. Res. 136 (2020) 106159, https://doi.org/10.1016/j.cemconres.2020.106159.

[145] H. Tran, A. Scott, R. Dhakal, Mechanical and durability properties of magnesium silicate hydrate binder concrete, Mag. Concr. Res. 72 (2020) 693–702, https://doi.org/10.1680/jmacr.18.00217.

[146] M. Dhakal, A.N. Scott, R.P. Dhakal, D. Clucas, Structural and durability properties for magnesia alumina silicate concrete, Construct. Build Mater. 340 (2022) 127725, https://doi.org/10.1016/j.conbuildmat.2022.127725.

[147] B. Lothenbach, F. Winnefeld, Thermodynamic modelling of the hydration of Portland cement, Cem. Concr. Res. 36 (2006) 209–226, https://doi.org/10.1016/j.cemconres.2005.03.001.

[148] A. Vollpracht, B. Lothenbach, R. Snellings, J. Haufe, The pore solution of blended cements: a review, Mater. Struct. 49 (2016) 3341–3367, https://doi.org/10.1617/s11527-015-0724-1.

[149] M. Adler, U. Mäder, N. Waber, High-pH alteration of argillaceous rocks: an Experimental Study, Schweiz. Mineral. Petrogr. Mitt. 79 (1999) 445–454.

[150] F. Claret, A. Bauer, T. Schäfer, L. Griffault, B. Lanson, Experimental investigation of the interaction of clays with high-pH solutions: a case study from the Callovo-Oxfordian formation, Meuse-haute Marne underground laboratory (France), Clay Clay Miner. 50 (2002) 633.

[151] A. Bauer, G. Berger, Kaolinite and smectite dissolution rate in high molar KOH solutions at 35° and 80°C, Appl. Geochem. 13 (1998) 905–916, https://doi.org/10.1016/S0883-2927(98)00018-3.

[152] S. Ramírez, J. Cuevas, R. Vigil, S. Leguey, Hydrothermal alteration of "La Serrata" bentonite (Almeria, Spain) by alkaline solutions, Appl. Clay Sci. 21 (2002) 257–269. doi:https://doi.org/10.1016/S0169-1317(02)00087-X.

[153] P. Lalan, A. Dauzères, L. de Windt, J. Sammaljärvi, D. Bartier, I. Techer, V. Detilleux, M. Siitari-Kauppi, Mineralogical and microstructural evolution of Portland cement paste/argillite interfaces at 70 °C – considerations for diffusion

and porosity properties, Cem. Concr. Res. 115 (2019) 414–425, https://doi.org/10.1016/j.cemconres.2018.09.018.

[154] U. Mäder, A. Jenni, C. Lerouge, S. Gaboreau, S. Miyoshi, Y. Kimura, V. Cloet, M. Fukaya, F. Claret, T. Otake, M. Shibata, B. Lothenbach, 5-year chemico-physical evolution of concrete–claystone interfaces, Mont Terri rock laboratory (Switzerland), Swiss J. Geosci. 110 (2017) 307–327, https://doi.org/10.1007/s00015-016-0240-5.

[155] T. Zhang, J. Zou, Y. Li, Y. Jia, C.R. Cheeseman, Stabilization/solidification of strontium using magnesium silicate hydrate cement, Processes 8 (2020) 163, https://doi.org/10.3390/pr8020163.

[156] T. Zhang, E. Dieckmann, S. Song, J. Xie, Z. Yu, C. Cheeseman, Properties of magnesium silicate hydrate (M-S-H) cement mortars containing chicken feather fibres, Construct. Build Mater. 180 (2018) 692–697, https://doi.org/10.1016/j.conbuildmat.2018.05.292.

[157] G.A. Douillet, N. Toropovs, W.J. Zucha, E. Bernard, A. Kühnis, F. Schlunegger, The compressive strength of earth-hemp blocks tested with different densities, earth types, and cementitious binders, Copernicus Meetings (2022), https://doi.org/10.5194/egusphere-egu22-12781.

[158] T. Zhang, Z. Zhou, M. Li, Z. He, Y. Jia, C.R. Cheeseman, C. Shi, Effect of hydrated magnesium carbonate grown in situ on the property of MgO-activated reactive SiO$_2$ mortars, Journal of Sustainable Cement-Based Materials 11 (2022) 286–296, https://doi.org/10.1080/21650373.2021.1951880.

[159] A.N. Scott, C. Oze, Constructing Mars: concrete and energy production from serpentinization products, earth and space, Science 5 (2018) 364–370, https://doi.org/10.1029/2017EA000353.

[160] E. Bernard, B. Lothenbach, C. Chlique, M. Wyrzykowski, A. Dauzères, I. Pochard, C. Cau-Dit-Coumes, Characterization of magnesium silicate hydrate (M-S-H), Cem. Concr. Res. 116 (2019) 309–330, https://doi.org/10.1016/j.cemconres.2018.09.007.

[161] R. Huang, L. He, T. Zhang, D. Li, P. Tang, Y. Zhao, Y. Feng, Fabrication and adsorption behavior of magnesium silicate hydrate nanoparticles towards methylene blue, Nanomaterials (Basel) 8 (2018) 271, https://doi.org/10.3390/nano8050271.

[162] S. Han, L. Mao, H. Wang, Preparation of magnesium silicate/polyethersulfone hybrid ultrafiltration membrane for macromolecular intercept and dye removal,

Desalin. Water Treat. 105 (2018) 298–309, https://doi.org/10.5004/dwt.2018.21984.

[163] Z. Zhao, Z. Li, P. Cui, S. Li, L. Kong, Adsorption of basic Brown and Chrysophenine from water solution by magnesium silicate gel, J. Chem. 2015 (2015) e374190, https://doi.org/10.1155/2015/374190.

[164] H. Yang, B. Sun, H. Wang, Removal of anionic dye from aqueous solution by magnesium silicate gel, Desalin. Water Treat. 52 (2014) 7685–7692, https://doi.org/10.1080/19443994.2013.831779.

[165] T.F. Kuznetsova, A.I. Ivanets, L.V. Kul'bitskaya, N.L. Budeiko, Yu.D. Savka, Synthesis and characterization of homogeneously mesoporous magnesium silicates with prospects of application in catalysis and adsorption, Prot. Met. Phys. Chem. Surf. 53 (2017) 651–656. doi:https://doi.org/10.1134/S2070205117040116.

[166] Z. Li, Q. Yu, X. Chen, H. Liu, J. Zhang, J. Zhang, Y. Yang, J. Wei, The role of MgO in the thermal behavior of MgO–silica fume pastes, J. Therm. Anal. Calorim. 127 (2017) 1897–1909, https://doi.org/10.1007/s10973-016-5827-6.

[167] S. Zhang, N. Liao, Y. Li, A. Chatterjee, Y. Zhang, S. Sang, M- S-H formation in MgO-SiO$_2$ slurries via wet milling for magnesia based castables, Ceram. Int. 47 (2021) 10880–10886, https://doi.org/10.1016/j.ceramint.2020.12.207.

[168] M. Dhakal, A.N. Scott, V. Shah, R.P. Dhakal, D. Clucas, Development of a MgO-metakaolin binder system, Construct. Build Mater. 284 (2021) 122736, https://doi.org/10.1016/j.conbuildmat.2021.122736.

[169] C. Sonat, S. He, J. Li, C. Unluer, E.-H. Yang, Strain hardening magnesium-silicate-hydrate composites (SHMSHC) reinforced with short and randomly oriented polyvinyl alcohol microfibers, Cem. Concr. Res. 142 (2021) 106354, https://doi.org/10.1016/j.cemconres.2021.106354.

[170] G. Mármol, H. Savastano, Study of the degradation of non-conventional MgO-SiO$_2$ cement reinforced with lignocellulosic fibers, Cement and Concrete Composites 80 (2017) 258–267, https://doi.org/10.1016/j.cemconcomp.2017.03.015.

[171] M. Dhakal, A.N. Scott, R.P. Dhakal, T.J. Sullivan, D. Clucas, Performance of MgO-Mk based MSH concrete column reinforced with steel and BFRP bars under cyclic loads, Structures 46 (2022) 1764–1780, https://doi.org/10.1016/j.istruc.2022.11.025.